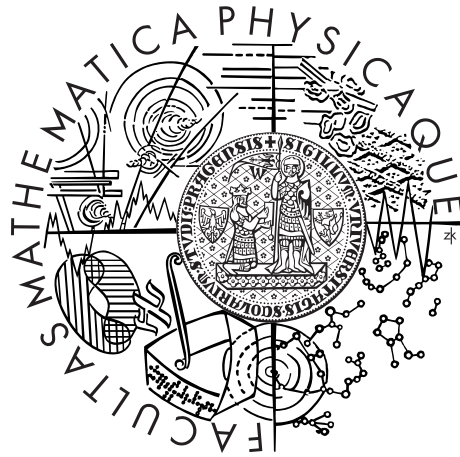Charles University in Prague

Faculty of Mathematics and Physics

MASTER THESIS

Vojtěch Vozda

Advanced simulations of photonic structures by FDTD method

Institute of Physics of Charles University

Supervisor of the master thesis:	RNDr. Martin Veis, Ph.D.
Study programme:	Physics
Specialization:	Optics and optoelectronics

Prague 2015

I declare that I carried out this master thesis independently, and only with the cited sources, literature and other professional sources.

I understand that my work relates to the rights and obligations under the Act No. 121/2000 Coll., the Copyright Act, as amended, in particular the fact that the Charles University in Prague has the right to conclude a license agreement on the use of this work as a school work pursuant to Section 60 paragraph 1 of the Copyright Act.

In .... date ....   signature of the author

Název práce: Pokročilé simulace fotonických struktur metodou FDTD

Autor: Vojtěch Vozda

Katedra: Fyzikální ústav UK

Vedoucí diplomové práce: RNDr. Martin Veis, Ph.D., Fyzikální ústav UK

Abstrakt: Metoda konečných diferencí v časové doméně (Finite-Difference Time-Domain method - FDTD) vychází z numerického řešení Maxwellových rovnic a v dnešní době je často používána k simulaci optické odezvy od fotonických struktur. Tato práce poskytuje rychlý úvod do FDTD a několika nejdůležitějších rozšíření, které ji činí velmi univerzální. Z důvodu získání podrobnější analýzy fotonických struktur, je zde také zmíněna metoda matic přenosu (transfer matrix method - TMM). Kód je nejdříve otestován na jednoduchý strukturách, kde může být řešení porovnáno s jinými, ať už numerickými či analytickými metodami. Odladěný kód je použit na vylepšení fotonických krystalů užitých pro zvýšení citlivosti biosenzorů založených na změně indexu lomu zkoumané látky. V neposlední řadě jsou zkoumány vlastnosti (citlivost a Q-faktor rezonančního maxima) děrovaného vlnovodu v jedno-, dvou- a tří-dimenzionální simulaci. Je ukázáno, že i tato jednoduchá struktura může na poli biosenzorů soupeřit s komplexními fotonickými krystaly.

Klíčová slova: FDTD, TMM, fotonické struktury, biosensory

Title: Advanced simulations of photonic structures by FDTD method

Author: Vojtěch Vozda

Department: Institute of Physics of Charles University

Supervisor: RNDr. Martin Veis, Ph.D., Institute of Physics of Charles University

Abstract: Finite-Difference Time-Domain method (FDTD) is based on numerical solution of Maxwell's equations, nowadays widely used for simulating optical response of photonic structures. This paper provides brief introduction to the FDTD method and several important extensions which make the basic code much more versatile. In order to broaden analysis of photonic structures, transfer matrix method (TMM) is also involved. The code is firstly tested using simple model structures which optical response might be compared with different numerical or even analytical approaches. Debugged code is used to improve photonic crystals for enhanced sensitivity of biosensing devices based on refractive index changes of sensed medium. Last but not the least, properties (sensitivity and Q-factor of resonant peak) of holey waveguide are investigated in one-, two- and three-dimensional simulation. It is shown here, that even this simple structure may compete with complex photonic crystals in the field of biosensors.

Keywords: FDTD, TMM, photonic structures, biosensors

Contents

Introduction

Looking into the history, our progression is based on studying features of new and newer materials. Step by step, ancient people learn how to use stones, iron, bronze and many more alloys. Extremely fast development of last few decades is based on controlling electrical properties of materials and electron behaviour which results in extremely powerful computational machines — computers. Using computers we can solve unthinkable problems which requires billions of operations which simply cannot be solved on a paper with a common pencil. Thus, we can design and control many sophisticated materials, robots, cars and other gadgets which make our living much more simple, comfortable and contribute to overall progress.

Now, we are able to control movement of electrons and probably the next goal might be figuring out how to control optical properties and propagation of light particles — photons. As we acquire this knowledge, we will be able to engineer materials with desired optical response which could result in perfect reflection of required range of frequencies, light propagation in certain direction or even in *all-optical* computers.

These revolutionary computers would use light signals instead of electronic. The great difference is that photons do not produce heat while propagating in waveguides. Therefore we could overclock our processors to higher frequencies without any fear we will burn them. Although we had already entangled Earth by fibre-optic cables which revolutionized the telecommunications industry, the idea of all-optical computer is still far beyond any commercial applications. Nevertheless, using sophisticated structures like *photonic crystals*, we are able to design optical analogies to well known electronic diodes, transistors, switches, etc. On the other hand, many of them uses nonlinear approaches which require high-power input source due to small nonlinear susceptibility coefficient. Thus, a lot of energy must be pumped into optical chips.
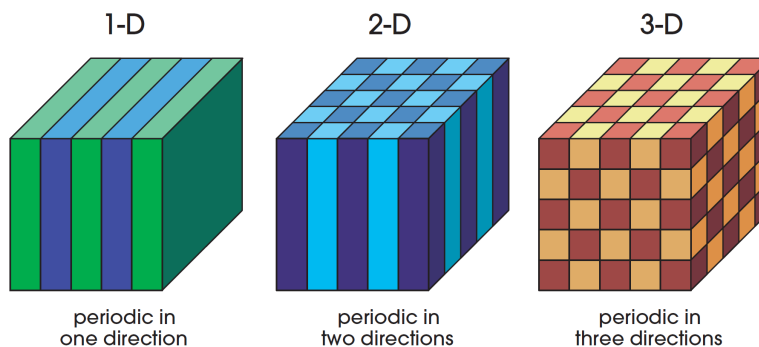

Figure 1: Schematic diagrams illustrating contrast between photonic crystals of different dimensions. Colours correspond to materials with various optical properties. Only periodicity in all three directions can support an omnidirectional photonic band gap. However, more complex topology, than shown here, is needed. Taken from [1].

Photonic crystals

Nowadays, quantum mechanics explains strange and non-trivial physical properties of crystals without any difficulty. The periodic potential in semiconductor crystals affect electron motion by defining allowed and forbidden energy bands. Electrons with certain energy may therefore propagate through the crystal almost like free particles in a free space. Since electrons behave as waves at these energies, we may expect that the propagation of photons in periodic dielectric structures would be driven by similar rules. The periodic photonic structures are usually called *photonic crystals* (PhC). Figure 1 illustrates PhCs which are periodical along one, two and three axes. These special structures affect propagation of electromagnetic waves in very similar manner as semiconductor crystals affect electron motion. Instead of valence and conduction bands here we define here dielectric and air bands. If we take a deeper look into the mathematical theory, we may find out, that Schrödinger's equation describing electron movement is very similar to eigenvalue problem in electromagnetism, which follows from Maxwell's equations. Therefore, we can find many problems which have analogous solution in quantum mechanics (QM) and electromagnetism (EM) [1].

Notable difference between QM and EM problems is that Maxwell's equations do not have any fundamental scale[(1)]. The crucial is just ratio of structure size and wavelength of propagating light. This makes PhCs scalable in a way that ordinary crystals are not. Hence, the simulations might be done in arbitrary units and after that scaled to particular incident wavelength or characteristic dimensions. In QM problem is scale set via Louis de Broglie's electron wavelength, binding energy, atom size, etc.

The one-dimensional PhCs and dielectric multilayers have been studied since 1887 when Lord Rayleigh showed that such structures has a 1D-photonic *band gap*. This is a range of frequencies at which the propagation of electromagnetic waves is not allowed. Nevertheless, the term 'photonic crystal' was first used 100 years later in 1987 when E. Yablonovitch and S. John published two milestone papers on these periodic structures [2], [3]. Yablonovitch's main motivation was the control of spontaneous emission, which plays a fundamental role in the limitation of the performance of semiconductor lasers or solar cells. On the other hand John suggested to use PhCs for localization and control of photons.

Figure 2: SEM photograph of photonic crystal fibre. The solid core of fibre is 5μm. Provided by US Naval Research Laboratory.

After publishing these two papers, the number of publications concerning PhCs began to grow exponentially. The first experimental confirmation of photonic gap has been done in microwave regime, for which the PhCs can be fabricated more easily than for optical regime. The first experiment at optical frequencies was demonstrated by Thomas Krauss in 1996, [4]. In
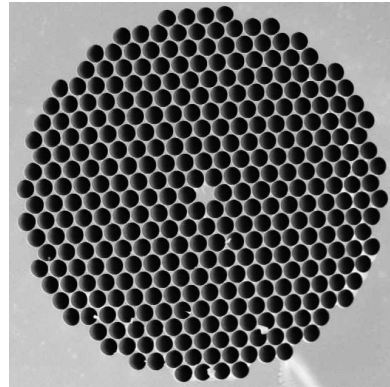
---

[1]It is not valid for dispersive materials, which affect light propagation at various wavelengths in different ways.

1998 Philip Russell et.al. developed photonic crystal fibre, which offered many degrees of freedom in its design resulting in desired optical properties. Figure 2 shows photograph of photonic crystal fibre from scanning electron microscope. This fibre has a totally different guiding mechanism than ordinary optical fibres based on photonic band gap of the cladding.

The interest in materials with photonic band gap arises from their potential applications in novel optical devices, such as filters, waveguides, cavities, design of more efficient lasers, etc. One of these novel concepts might be useful for biosensing.

Biosensing

Many experimental optical methods and approaches like ellipsometry, interferometry, surface plasmonic resonance and other were adapted for detection of biochemical reactions during last two decades. Biosensors are important for drug discovery, protein or disease detection, for DNA analysis. The critical properties are compactness, high sensitivity, simple fabrication and compatibility with other optical or electronic elements.

Biosensors based on refractive index (RI) change detect optical response of nanostructures upon the presence of investigated medium. Two main approaches are plasmonic and photonic structures. Plasmonic structures utilize effect known as *surface plasmon resonance* (SPR). In principle, they sense RI changes near a metal surface by measuring the changes of reflectance due to the modified coupling of incident light to surface plasmons. These structures are, however, facing critical properties like low compactness, difficult fabrication or integration with other optical components. The photonic structures get rid of all these imperfections. In fact, these issues are actually their preferences. Photonic structures exhibit dispersion relations which are highly sensitive on RI changes of investigated medium, which is applied on the surface or inside the perforated structure. The method of monitoring RI changes is based on observing cut-off wavelengths (the edge of the band gap) or resonant peak position [5].

Numerical approaches

The analytical methods for the calculation of PhC's band structures have been reported, but does not provide us full understanding of all useful features of these exceptional materials [6]. Thus, many complementary numerical approaches have been proposed to investigate properties of photonic crystals more precisely. Here we briefly introduce just few of them.

One of the most intuitive approaches adapted to compute optical response of stack of homogeneous thin films with different RI (multilayer) is Transfer matrix method (TMM). The formalism of TMM for multilayers was first proposed by F. Abelès in 1950 [7]. It is based on numerical calculation of Fresnel equations, which describe the reflection and transmission of light from a single interface between two media. The formalism can be derived by combining Fresnel equations with electromagnetic field propagation in homogeneous layers and continuity of the tangential components of EM field at the interfaces. The primary output of TMM is reflection and transmission spectrum, but dispersion relations of infinite

periodic structure can be obtained as well. The simplicity of TMM formalism is compensated by the use just for one-dimensional problems.

Thus two-dimensional numerical technique called Finite element method (FEM) was adapted to PhC modelling [8]. The FEM finds approximate solution to boundary value problems by dividing whole problem domain into simpler parts called finite elements and hence it can handle with complicated geometries with relative ease.

The very popular method for computing the band structure of PhCs with arbitrary variation of RI is Plane wave expansion (PWE) method which is adapted to solve eigenvalue problem formulated by Maxwell's equations. The method can deal with computation of eigenfrequencies and eigenmodes of large size problems. However, it requires computation of eigenvalues of large matrices, which takes a lot of computational resources (memory and time), and for scattering analysis it can be used just with non-trivial modifications.

All methods mentioned above have one in common. Whether we compute transmission spectrum or dispersion relations, we compute it for one given frequency — we are talking about frequency domain methods which study behaviour of monochromatic wave propagation. Naturally, the opposite are time domain methods. The most used method in this field is Finite difference time domain method (FDTD), which has been first proposed by Kane Yee in 1966 [9]. This method solves Maxwell's equations in the time domain on a discrete lattice (called Yee grid) which represents real space. Since the simulation runs in our common space-time and does not use any abstract frequency domain, it can provide better understanding of light propagation, for example via animated output. The frequency output is obtained via discrete Fourier transform (DFT) for all desired frequencies at once, if a broadband pulse is used as a source. This is very useful in applications where resonant frequencies are not exactly known or computation of broadband spectrum is necessary. The other advantages of FDTD are its simplicity and versatility. Basic algorithm, which uses miscellaneous extensions, can deal with time-varying, anisotropic, lossy, dispersive and nonlinear media [10].

Outline of the thesis

The main aim of this work is to present complex results from 3D-FDTD simulations showing biosensing potentials of holey waveguide. To understand it properly, we provide here brief theoretical introduction to FDTD theory supplemented with model examples which inconspicuously contribute to completeness of the holey waveguide model.

In the Chap. 1, we firstly acquaint ourselves with numerical integration, which is an essential and integral part of FDTD. Secondly, we derive Yee algorithm from Maxwell's equations and provide short description of the most popular FDTD extensions. After that, we also provide an introduction into the TMM, which will be further used to compare and extend results obtained from FDTD.

Chapter 2 presents some simple structures where the results can be compared with analytical solution, and thus the correctness of the simulation algorithm is confirmed. We examine reflection of an inhomogeneous dielectric step by TMM and FDTD, than we take a look at a near-field of Gaussian pulse scattered on a grating. After that we use characteristic equation to describe eigenmodes in

symmetrical plane waveguide, which will be useful when modelling photonic structures. The functionality of the FDTD code in three-dimensions is demonstrated on diffraction problem using circular aperture and comparison with Fresnel diffraction.

After equipping ourselves with the appropriate theoretical tools and verifying FDTD algorithm we attempt to propose novel photonic structures with high potential use as biosensors based on RI changes. Firstly, in Chap. 3, we enhance hexagonal PhC for biosensing by introducing additional holes in its middle row, which represents a waveguide. Than we also show that crystal with broken periodicity, designed originally as an optical diode, exhibit very large sensitivity on RI changes. Secondly, in Chap. 4, we subject photonic structure known as holey waveguide to precise investigation of its parameters to show, that even such simple structure may compete with PhCs in the area of biosensors.

Finally, we conclude our work and results.

1. Theoretical prelude

Since the FDTD simulation is done in the common space and time, the results are very often understandable even without any detailed description. Nevertheless, if we want to obtain reasonable results, we should know what does the algorithm contain and what approximations have to be done before and during computation. Before we focus on the FDTD theory, let us briefly introduce the main idea of the algorithm which is the heart of FDTD.

1.1 Numerical integration

As a model example for solving ordinary differential equations, we investigate here behaviour of a classical harmonic oscillator. The particle mass is m, force constant k and time-dependant position is denoted by $x(t)$. The differential equation governing oscillator's dynamics is

$$\ddot{x}(t) = -\frac{k}{m}x(t) \quad \begin{cases} \dot{x}(t) &= v(t) \\ \dot{v}(t) &= -\frac{k}{m}x(t) \end{cases} \tag{1.1}$$

To study the system numerically, we rewrote the second-order differential equation as two coupled first-order equations. The velocity of the oscillator is denoted by $v(t)$, and $\dot{v}(t) = a(t)$ denotes the acceleration. To integrate these equations we discretize continuous time-axis into many discrete points $t = t_0, t_1, \ldots$, with a constant time-step $\Delta_t = t_{n+1} - t_n$. The initial values of the oscillator are defined in $t = t_0$ as x_0 and v_0.

Let's rewrite the set of equations (1.1) to make them understandable even for computers in the most intuitive way

$$a_{n+1} = -\frac{k}{m}x_n, \tag{1.2a}$$

$$x_{n+1} = x_n + \Delta_t v_n, \tag{1.2b}$$

$$v_{n+1} = v_n + \Delta_t a_{n+1}, \tag{1.2c}$$

where the low indices stand for time steps (i.e. $x_n = x(n\Delta_t) = x(t_n)$). When computer proceeds this algorithm, it will evaluate a_1 from the initial value x_0 using (1.2a), then x_1 from x_0 and v_0 using (1.2b), next v_1 from v_0 and a_1 using (1.2c), after that it will go back to the first equation and compute the cycle again until we will be satisfied with the results. The described procedure is called *Euler's algorithm*.

In general, this algorithm is not very useful in practice because the error $\mathcal{O}(\Delta_t^2)$ cumulates in each step and solution is not stable. Figure 1.1 illustrates the phase space of the oscillator with $m = 1\text{kg}$, $k = 1\text{kg·s}^{-2}$, $x_0 = 1\text{m}$, $v_0 = 0$. Since the motion is periodical, the trajectory in the phase space should be a closed curve and not the spiral we have obtained. It shows the numerical solution is not correct.

How can we improve the algorithm to get more physical results? We compute the Taylor expansion of $x_{n\pm1} = x(t_n \pm \Delta_t)$

Figure 1.1: The phase space of harmonic oscillator. If the solution would be correct, we should see a closed curve and not the widening spiral. This example clearly illustrates the Euler's method is not stable.
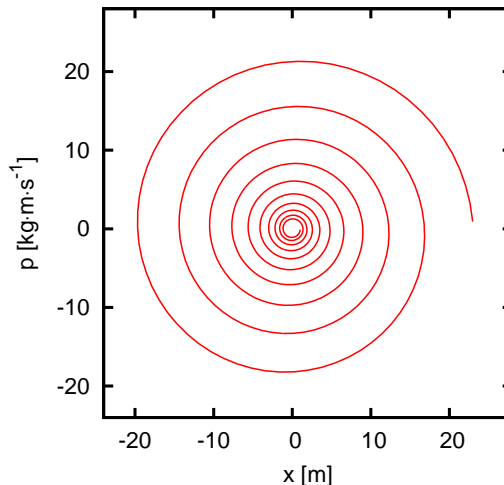
$$x(t_n \pm \Delta_t) = x(t_n) \pm \Delta_t \dot{x}(t_n) + \frac{1}{2}\Delta_t^2 \ddot{x}(t_n) \pm \frac{1}{6}\Delta_t^3 \dddot{x}(t_n) + \mathcal{O}(\Delta_t^4) =$$
$$= x(t_n) \pm \Delta_t v(t_n) + \frac{1}{2}\Delta_t^2 a(t_n) \pm \frac{1}{6}\Delta_t^3 \dot{a}(t_n) + \mathcal{O}(\Delta_t^4).$$

Adding these two equations yields

$$x_{n+1} = 2x_n - x_{n-1} + \Delta_t^2 a_n + \mathcal{O}(\Delta_t^4), \tag{1.3}$$

which is called *Verlet algorithm*. Noting the fact that $x_n - x_{n-1} = \Delta_t v_{n-1/2}$ and $v_{n+1/2} - v_{n-1/2} = \Delta_t a_n$ we get a *leapfrog method*, which is in fact identical to Verlet's

$$v_{n+\frac{1}{2}} = v_{n-\frac{1}{2}} + \Delta_t a_n, \tag{1.4a}$$

$$x_{n+1} = x_n + \Delta_t v_{n+\frac{1}{2}}, \tag{1.4b}$$

$$a_{n+1} = -\frac{k}{m}x_{n+1}. \tag{1.4c}$$

The main idea of the leapfrog algorithm is that we compute the velocity v and the position x at different grid points. We even do not know what is the position and the velocity of the particle at the same time. Furthermore, we have to adjust initial condition v_0 to $v_{-1/2}$. It seems to be unnecessarily complicated, but the results are more than satisfying.

Figure 1.2 compares Euler and leapfrog methods showing the evolution of oscillator's energy in time for two different time-steps Δ_t. As the figure indicates, the solution obtained by Euler method is non-physical because the oscillator's energy is diverging, although no force is acting on it. If we decrease the time step, we will get better behaviour but only for short times. The solution would diverge anyway if we computed simulation for longer times. Yes, we can decrease time step more and more but then we also have to wait longer and longer for
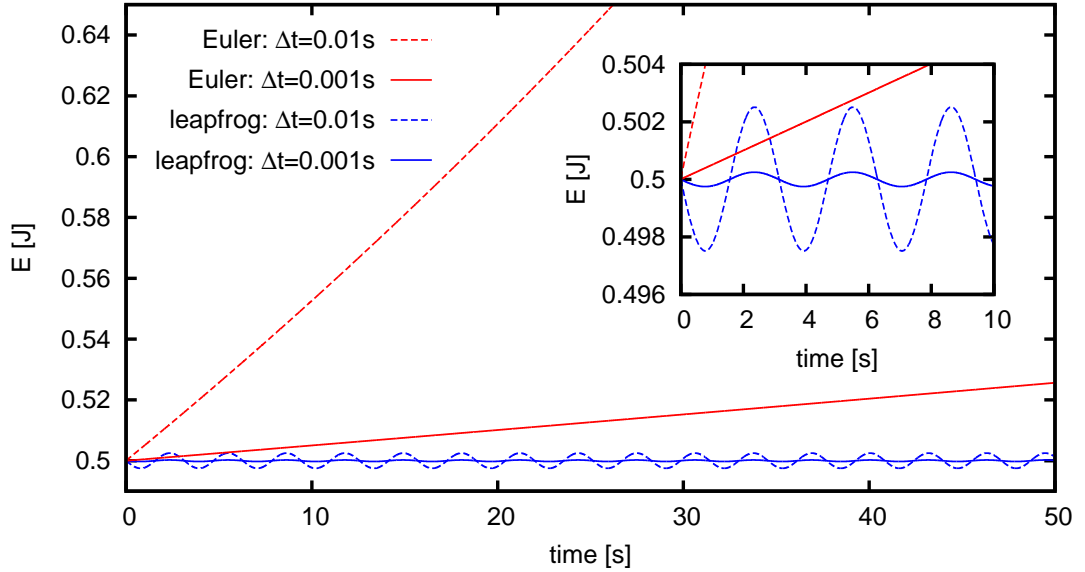
Figure 1.2: Time evolution of harmonic oscillator's energy computed by Euler and leapfrog method for different Δ_t. While the Euler method diverges, the energy obtained from leapfrog only oscillates. The inset illustrates zoom of the first ten seconds.

results, because computers are still not infinitely fast. It is clear that this way does not lead us to any significant breakthrough.

The situation seems to be much better when leapfrog algorithm is used. Energy oscillates around the correct value 0.5J but does not diverge. The smaller Δ_t we use, the smaller oscillations we get. Moreover, the leapfrog algorithm is time-reversible, i.e., we can move back and forth in time without any decrease of precision (up to numerical round-off errors). This feature can be used to check the sensitivity of simulation to round-off errors.

1.2   Finite Difference Time Domain

Since we are about to describe light, the electromagnetic waves, we should begin with *Maxwell's equations*. This set of equations is named after the Scottish physicist and mathematician James Clerk Maxwell, who formulated their early form of those equations about 1861 [11]

$$\nabla \cdot \mathbf{D} = \rho \qquad \text{(Gauss's law)}, \tag{1.5a}$$

$$\nabla \cdot \mathbf{B} = 0 \qquad \text{(Gauss's law for magnetism)}, \tag{1.5b}$$

$$\nabla \times \mathbf{E} = -\frac{\partial \mathbf{B}}{\partial t} - \mathbf{M} \qquad \text{(Faraday's law of induction)}, \tag{1.5c}$$

$$\nabla \times \mathbf{H} = \mathbf{j} + \frac{\partial \mathbf{D}}{\partial t} \qquad \text{(Maxwell-Ampère's circuital law)}, \tag{1.5d}$$

where $\mathbf{E}$ is the electric field, $\mathbf{D}$ is the electric flux density, $\mathbf{H}$ is the magnetic field, $\mathbf{B}$ is the magnetic flux density, $\mathbf{j}$ is the current density, $\mathbf{M}$ is the magnetic current density and ρ denotes the charge density.

11

If we consider wave propagation in linear isotropic and non-dispersive material, the constitutive relations are

$$\mathbf{D} = \varepsilon\mathbf{E}, \tag{1.6a}$$

$$\mathbf{B} = \mu\mathbf{H}, \tag{1.6b}$$

where ε is permittivity and μ permeability. In free space they are defined as

$$\varepsilon = \varepsilon_r\varepsilon_0 = \varepsilon_0 \approx 8,854 \times 10^{-12}\mathrm{F}\cdot\mathrm{m}^{-1}, \tag{1.7a}$$

$$\mu = \mu_r\mu_0 = \mu_0 = 4\pi \times 10^{-7}\mathrm{H}\cdot\mathrm{m}^{-1}, \tag{1.7b}$$

where ε_r and μ_r denote relative permittivity and permeability, respectively. The electric current density $\mathbf{j} = \sigma^e\mathbf{E}$ and σ^e is the electric conductivity. Similarly, $\mathbf{M} = \sigma^m\mathbf{H}$, σ^m is the magnetic conductivity. For the simplicity, all materials will be considered as non-magnetic, unless otherwise stated. Therefore, the refractive index is $n = \sqrt{\varepsilon}$, since $\mu_r = 1$.

1.2.1   Yee's algorithm in 3D

As the abbreviation FDTD (Finite-Difference Time-Domain) prompts, FDTD is the method which solves Maxwell's equations in the time domain. The method was first used by Kane Yee for analysis of two-dimensional scattering problem of magnetic pulses from rectangular cylindrical conductors [9]. Although Yee proposed the method in 1966, it did not gain popularity until mid-seventies when computers became fast enough to deal with large amount of operations which FDTD requires. In the beginning it was used in the area of microwave and millimetre-wave research. With faster and more powerful computers the method was applied little by little on more complex problems.

Nowadays, the FDTD is widely used to design antennas, microwave filters, scattering structures or even PhCs. On the other hand, FDTD is restricted to problems, which are comparable with wavelength of propagating light. If the objects were too small compared to wavelength (e.g. tiny quantum dots versus visible light), it would be better to use quasistatic approximations. If objects were too large (e.g. laser beam propagating through some lenses and polarisers placed on optical table), it would be better to use approaches based on geometrical optics. Otherwise, we would probably require extremely large computational grid and integration over so many time steps, that we would wait years and years for results.

Since the FDTD is time domain simulation, we do not have to work with such abstract terms like Brillouin zone, dispersion relations or eigensystem[1], although we will talk about periodic structures like PhCs. Instead of that, we discretize the real continuous space-time into discrete counterparts. Then, geometry of the investigated problem might be easily stored into large arrays or matrices in computer's memory. After that, we define matrices of the same sizes

---

[1] Computation of dispersion relations with FDTD is possible, but similar to cracking a nut with a sledgehammer.

for electromagnetic field, which are updated in time-marching loop using Yee's leapfrog algorithm step by step.

Instead of writing down, or even deriving, all equations and sophisticated methods which build and improve the FDTD code, we rather refer the inquisitive reader to the literature [10, 12, 13, 14, 15, 16]. Here we explain only the bare essentials.

The Yee's algorithm is as follows:

1. Replace all the derivatives in Ampère's (1.5d) and Faraday's (1.5c) laws with finite differences. Discretize space and time so the electric and magnetic fields are separated in both space and time.

2. Solve the difference equations to obtain *update equations* that express the unknown future fields in term of known past fields.

3. Using the update equations enumerate future magnetic fields.

4. Using the update equations enumerate future electric fields.

5. Repeat last two steps unless you are satisfied with the results.

Let's see what is hidden behind these *update equations* in three dimensional case. As the Yee's algorithm postulates, Ampère's (1.5d) and Faraday's (1.5c) laws are the governing equations in constructing the FDTD. Breaking down the curl of $\mathbf{E}$ and $\mathbf{H}$ we get

$$-\sigma^m \mathbf{H} - \mu \frac{\partial \mathbf{H}}{\partial t} = \nabla \times \mathbf{E} = \begin{vmatrix} \hat{\mathbf{e}}_x & \hat{\mathbf{e}}_y & \hat{\mathbf{e}}_z \\ \partial_x & \partial_y & \partial_z \\ E_x & E_y & E_z \end{vmatrix}, \tag{1.8a}$$

$$\sigma^e \mathbf{E} + \varepsilon \frac{\partial \mathbf{E}}{\partial t} = \nabla \times \mathbf{H} = \begin{vmatrix} \hat{\mathbf{e}}_x & \hat{\mathbf{e}}_y & \hat{\mathbf{e}}_z \\ \partial_x & \partial_y & \partial_z \\ H_x & H_y & H_z \end{vmatrix}. \tag{1.8b}$$

Now we have to replace derivatives. We use the central difference formula with the error $\mathcal{O}(\Delta_x^2)^{(2)}$

$$\frac{\mathrm{d}f(x)}{\mathrm{d}x} \approx \frac{f(x + \Delta x) - f(x - \Delta x)}{2\Delta x}. \tag{1.9}$$

For the discretization we use notation similar to the harmonic oscillator in previous chapter

$$E_x(x, y, z, t) = E_x\left((m - 1/2)\Delta_x, (n - 1)\Delta_y, (p - 1)\Delta_z, q\Delta_t\right) = E_x^q[m, n, p],$$
$$E_y(x, y, z, t) = E_y\left((m - 1)\Delta_x, (n - 1/2)\Delta_y, (p - 1)\Delta_z, q\Delta_t\right) = E_y^q[m, n, p],$$
$$E_z(x, y, z, t) = E_z\left((m - 1)\Delta_x, (n - 1)\Delta_y, (p - 1/2)\Delta_z, q\Delta_t\right) = E_z^q[m, n, p],$$
$$H_x(x, y, z, t) = H_x\left((m - 1)\Delta_x, (m - 1/2)\Delta_y, (p - 1/2)\Delta_z, q\Delta_t\right) = H_x^q[m, n, p],$$
$$H_y(x, y, z, t) = H_y\left((m - 1/2)\Delta_x, (m - 1)\Delta_y, (p - 1/2)\Delta_z, q\Delta_t\right) = H_y^q[m, n, p],$$
$$H_z(x, y, z, t) = H_z\left((m - 1/2)\Delta_x, (m - 1/2)\Delta_y, (p - 1)\Delta_z, q\Delta_t\right) = H_z^q[m, n, p],$$

---

[2]More about other difference schemes, errors and precise analysis about all this non-trivial stuff can be find in [13].

Figure 1.3: Arrangement of the field components on the Yee cell indexed as $[m, n, p]$. Red arrows denote the electric field, blue arrows the magnetic one. The relative permittivity ε_x is at the same place as E_x, ε_y at the same place as E_y, etc. This arrangement is crucial when deriving the updating equations (1.11). It is also useful when sub-cell averaging is being involved into the computer code (section 1.2.2).
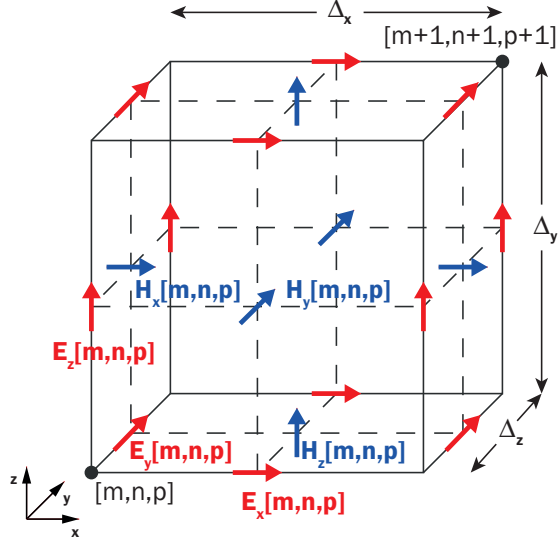
where indices m, n, p are related to positions in matrices. The arrangement of the fields illustrates Fig. 1.3.

In order to save the forests, we mention only one of six update equations. This can be derived from (1.8b) after some manipulations

$$
\begin{aligned}
E_x^{q+1}[m, n, p] = {} & \frac{2\varepsilon_x[m, n, p] - \Delta_t \sigma_x^e[m, n, p]}{2\varepsilon_x[m, n, p] + \Delta_t \sigma_x^e[m, n, p]} E_x^q[m, n, p] \\
& + \frac{2\Delta_t}{\left(2\varepsilon_x[m, n, p] + \Delta_t \sigma_x^e[m, n, p]\right) \Delta_y} \\
& \times \left(H_z^{q+1/2}[m, n, p] - H_z^{q+1/2}[m, n-1, p] \right) \\
& - \frac{2\Delta_t}{\left(2\varepsilon_x[m, n, p] + \Delta_t \sigma_x^e[m, n, p]\right) \Delta_z} \\
& \times \left(H_y^{q+1/2}[m, n, p] - H_y^{q+1/2}[m, n, p-1] \right) \\
& - \frac{2\Delta_t}{2\varepsilon_x[m, n, p] + \Delta_t \sigma_x^e[m, n, p]} j_x^{n+1/2}[m, n, p].
\end{aligned}
\tag{1.11}
$$

The ε was treated as permittivity tensor. This update equation will be simplified significantly if non-conducting material ($\sigma^e = 0$) is assumed.

This relation is very nice indeed, but what will a computer actually do if it compiles the update equations and algorithm? Firstly, empty matrices of the dimensions ($m \times n \times p$) for the fields $\mathbf{E}$ and $\mathbf{H}$ are defined. Then, matrices of the same dimensions for permittivity, permeability and current densities are defined. In this step, particular geometry is involved to the computation. If we want to simulate free space, the matrices for permittivity and permeability will be filled only with number one, the current density matrices will be filled with zeros. If we want to simulate a scattering of light on a silicon ball, some values in the permittivity matrix will be equal to 3.5^2, since the refractive index of silicon is about $n_{Si} = 3.5$ for $\lambda = 1550$nm [17].

The "bare-bone" code of FDTD simulation is attached in Appendix.

1.2.2 FDTD extensions

The basic FDTD algorithm, as introduced in previous paragraphs, does not provide too valuable results. If we run the loop with the updating equations on computer, we will get just a visual output of a spherical wave closed in a metal box, which may scatter on some badly defined dielectric or magnetic object.

Here we briefly describe what does the definition of material geometry contain, how can we simulate infinite space, plane waves, how can be frequency-dependent spectra obtained from time-domain simulation, how can be the far-field computed or even how can be dispersive materials simulated.

Sub-cell averaging

First of all we describe, how to build objects into the Yee grid. The field arrangement in the Yee cell as illustrated in Fig. 1.3 prompts, that building objects will probably not so easy as it might appear.

The simplest improvement is sub-cell averaging. After creating material geometry by changing ones to ε_r in case of permittivity, we check and redefine values at boundaries. For instance, the material component $\varepsilon_z[m, n, p]$ is located in between four Yee cells. If we consider that the material in each of them is different, we will rather use the average value for this cell

$$\varepsilon_z[m, n, p] = \frac{\varepsilon_z[m, n, p] + \varepsilon_z[m - 1, n, p] + \varepsilon_z[m, n - 1, p] + \varepsilon_z[m - 1, n - 1, p]}{4}.$$
(1.12)

The advantage of this method is that objects are modelled with better resolution without increasing size of the Yee grid and memory requirements are therefore preserved.

We will obtain even better resolution if we involve the particular shape of modelled objects. For example, if boundary of a dielectric ball ($\varepsilon_{\text{ball}}$) in free space went through a Yee cell, the relative permittivity of this Yee cell would be

$$\varepsilon = \frac{V_{\text{ball}}\varepsilon_{\text{ball}} + (V_0 - V_{\text{ball}})}{V_0},$$
(1.13)

where V_{ball} and V_0 is the volume of the part of the ball in particular cell and volume of the Yee cell, respectively.

Boundary conditions

A significant problem of updating equation as stated in Eq. (1.11) is to enumerate future value $E_x^{q+1}[m, n, p]$ we need to know the value of $H_y^{q+1/2}[m, n, p - 1]$ and others. The problem will occur, if we want to enumerate $E_x^{q+1}[m, n, 1]^{(3)}$, since the value $H_y^{q+1/2}[m, n, 0]$ does not exist. Therefore we do not update $E_x^{q+1}[m, n, 1]$ and it remains zero. Electric field is always zero in perfect electric conductor (PEC, $\sigma^e \approx +\infty$). That is why the edges of the Yee grid totally reflect all light which impact them. This is a serious problem when simulation in free space should be done.

---

[3] Notation is related to *matlab*, where first element of array has index 1.

To simulate free space, absorbing boundary conditions (ABC) must be defined. The most used method is *perfectly matched layer* (PML), which was introduced by Jean-Pierre Berenger in 1994 [18]. The idea of original PML is to define a non-physical material at the edges which attenuates incoming waves. To model infinite dielectrics, dispersive, nonlinear and all other materials, so-called complex frequency-shifted PML, known as *convolutional perfectly matched layer* (CPML), was developed.

Other method which can be used at edges of computational area are periodical boundary conditions, which are widely used for periodical structures such as crystals.

Total-Field/Scattered-Field (TFSF)

Objects consist of materials have been located in the grid, boundary conditions defined, and now we would like to introduce light source and light propagation. A simple point source, which produces a spherical waves, can be defined by a strict condition $E^q[m, n, p] = f(q)$ placed between fourth and fifth step in Yee's algorithm, where $f(q)$ is an arbitrary time-dependent function, e.g. $f(q) = \sin(\omega q)$. Nevertheless, in many cases we would like to simulate an impact of plane wave. One can say, it's not a problem since we know the wavefronts of spherical wave are nearly planar when investigated far from the source. It is true, of course, but we do not want to allocate so large arrays in computer memory and even not to wait for wave propagation.

Instead of that, we can use method known as Total-Field/Scattered-Field and excite the plane wave directly into the Yee grid [12, Chap. 3.10]. Using TFSF we excite many nodes of the grid and correct fields at many others to ensure the wave does not propagate outside the TFSF region.

Discrete Fourier transform (DFT)

Simulation in time-domain is nice, intuitive, and might help to understand wave propagation better. Nevertheless, results in the time domain are not very useful, since the real detectors are not so fast to be able even compare the theory with experiment. Fortunately, Fourier transform which relates time-domain with frequency-domain and vice versa exists. Because we use computers which operate in the discrete world, we define discrete Fourier transform (DFT)

$$F(\mathbf{r}, \nu) \approx \sum_{n=1}^{N} f(\mathbf{r}, n\Delta_t) e^{-i2\pi t \Delta_t \nu} \Delta_t, \tag{1.14}$$

where $F(\mathbf{r}, \nu)$ is the Fourier transform of function $f(\mathbf{r}, t) = f(\mathbf{r}, n\Delta_t)$. The smaller integration step Δ_t we use, the more accurate solution the transform produces.

When applied to FDTD, we use $\mathbf{E}(\mathbf{r}, t)$ and $\mathbf{H}(\mathbf{r}, t)$ as $f(\mathbf{r}, t)$ to calculate $\mathbf{E}(\mathbf{r}, \nu)$ and $\mathbf{H}(\mathbf{r}, \nu)$. In post-process we use these values to compute frequency-dependant Poynting vector $\mathbf{S}(\mathbf{r}, \nu)$

$$\mathbf{S}(\mathbf{r}, \nu) = \frac{1}{2} \mathbf{E}(\mathbf{r}, \nu) \times \mathbf{H}^*(\mathbf{r}, \nu), \tag{1.15}$$

from which the power flow $P_{\text{det}}(\nu)$ through some detector could be obtained easily

$$P_{\text{det}}(\nu) = \Re \left\{ \sum_{\text{det.}} \left(\mathbf{S}(\mathbf{r}, \nu) \cdot \mathbf{n} \right) \Delta_x \right\}, \tag{1.16}$$

where unit vector $\mathbf{n}$ is normal to the detector.

For instance, transmission spectrum of a three-dimensional waveguide in direction of z-axis might be obtained as

$$T(\nu) = \frac{P_1(\nu)}{P_2(\nu)}, \tag{1.17}$$

$$P_j(\nu) = \Re \left\{ \sum_{x=x_{\min}}^{x_{\max}} \sum_{y=y_{\min}}^{y_{\max}} S_z(x, y, z_j, \nu) \Delta_y \Delta_x \right\}; \qquad j = 1, 2 \tag{1.18}$$

where $x_{\min}$, $x_{\max}$, $y_{\min}$, $y_{\max}$ are edges of the waveguide and indices 1 and 2 correspond to two detectors at z-positions z_1 and z_2. Incident and transmitted power flows $(P_1\ P_2)$ are computed there.

Near-Field to Far-Field transformation (NTFF)

FDTD is method which computes the near-field, i.e., the field in the vicinity of scattering objects. But there are many situations (such as antenna radiation, grating diffraction, etc.) where we would like to know, how does the scattered field appears far away from the sources — in the far-field. One possible way is to define very large computational domain and wait years for results. Instead, the electromagnetic field far away from modelled objects is usually computed using the near-field to far-field transformation technique.

We enclose the antenna or any other scattering object into an imaginary surface and compute equivalent surface currents $\mathbf{J}$ and $\mathbf{M}$, which are determined by $\mathbf{E}$ and $\mathbf{H}$ computed inside the enclosed area. From the surface currents we compute electromagnetic field far away from the sources for all angles and selected number of frequencies [13].

Dispersive media in FDTD

As mentioned several times above, the FDTD method is not restricted only to linear and isotropic media.

The electromagnetic properties of materials depend more or less upon the frequency. Since the FDTD is time-domain method, it is evident that some advanced algorithms must be used to obtain more realistic optical response of materials. There are several analytical models which describe frequency dependence of materials. Two most common are Lorentz model for dielectrics and Drude model for metals. The leading approach used to model dispersive materials is known as *auxiliary differential equation* (ADE) method.

As the abbreviation prompts, the FDTD algorithm employs one additional differential equation. That consists of calculation of a polarization current, which is used to update the electric field with a slightly modified update equations.

1.2.3 Advanced meshes

The FDTD method as proposed above, provides efficient numerical algorithms for design and analysis of many structures. The main limitation of FDTD is its restriction to orthogonal grids, which means, the computational domain typically consists of a union of cubes. This causes many problems leading to smaller accuracy when curved surfaces or tiny structures are modelled. Such situations are common when quantum dots, small apertures or thin metal films have to be defined in the grid. The maximum improvement is possible when both space and time grid refinements are used. Many techniques have been proposed to extend basic Yee algorithm with inefficient staircase orthogonal meshes.

The simplest method uses more overlapping orthogonal grids with different space steps. For example, the space step around the nanoscale particle is small enough to describe its shape, whereas the space step in homogeneous space is bigger to obtain results in real time. These grids overlap typically about three cells [19].

How to solve Maxwell's equations in generalize nonorthogonal coordinates was first described by R. Holland in 1983 [20]. This approach was further developed up to current methods, which often uses combination of several schemes to achieve desired results [21]. The strength limitation of the methods is, that computational requirements grow a lot if algorithms are applied throughout the whole computational domain. Therefore, algorithms using nonorthogonal cells are preferred to be used only around the curved boundaries. Figure 1.4 compares several grids, which represent different approaches of grid refinement to particular geometry.

To ensure stability of FDTD algorithm, so-called *Courant-Friedrichs-Lewy* (CFL) condition must be fulfilled. In general form for non-orthogonal meshes it states [22]

$$\Delta t \leq \Delta t_{\max} = \begin{cases} \frac{1}{c\sqrt{\sum_{i,j}|g_{ij}|}} & \text{general non-orthogonal grid} \\[3ex] \frac{1}{c\sqrt{\frac{1}{(\Delta_x)^2}+\frac{1}{(\Delta_y)^2}+\frac{1}{(\Delta_z)^2}}} & \text{3D orthogonal grid} \end{cases} \quad (1.19)$$

where g_{ij} are the local matrix coefficients describing the nonorthogonality of the mesh. The condition simplifies a lot when the orthogonal mesh is used.

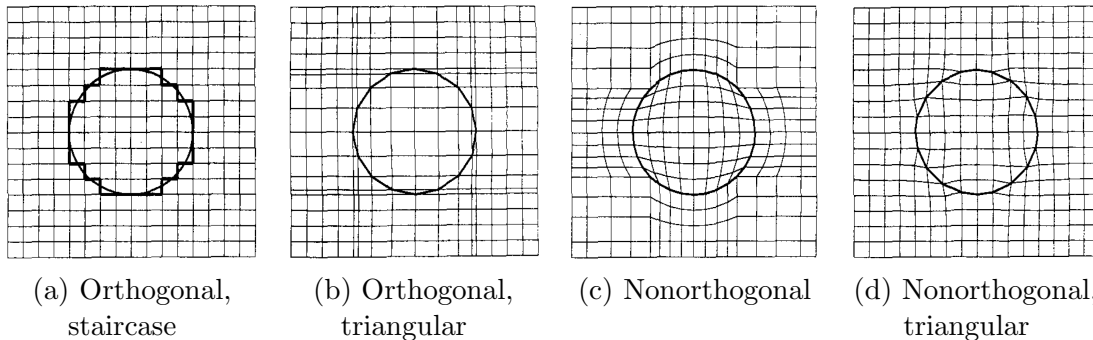| (a) Orthogonal, staircase | (b) Orthogonal, triangular | (c) Nonorthogonal | (d) Nonorthogonal, triangular |

Figure 1.4: Different grid refinements. The simplest case (a) was used in our FDTD algorithm. Pictures taken from [22].

The CFL condition provide us that the simulation is stable. Unfortunately, it does not mean no that no errors can occur. We used the central difference formula (1.9) with the error $\mathcal{O}(\Delta_x^2)$ to replace derivatives with finite differences. Due to this approximation, the numerical dispersion occurs. This is one of the main sources of inaccuracy. As non-orthogonal meshes are being employed into the algorithm, the numerical dispersion arises [23].

However, simulation in one dimension has a very nice feature known as a *magic time-step*. When we define $\Delta_t = \Delta_x/c$, all the errors will cancel and we will get exact numerical solution up to round-off errors. This is indeed very nice but unfortunately not too useful. The condition for magic time-step can be fulfilled only in free space, since the speed of light is dependent on the material. As Fig. 1.5 illustrates, numerical dispersion will occur if light propagates in dielectric material.

The numerical dispersion will be suppressed when better resolution is used. Here we define $N_\lambda = \lambda/\Delta_x$, which is the number of points per wavelength. The more precise our resolution is, the bigger N_λ is, and the smaller error caused by numerical dispersion occurs. In general, N_λ should be greater then 20 if we don't want to obtain any nonsense and greater than 50 to get more reasonable results.

The most simple case of non-uniform grid can be modelled in one dimension. Comparison with constant spatial step is shown in Fig. 1.5, where a simple interface between free space and dielectric material ($n = 3$) is modelled. In the case of non-uniform grid we define different spatial step for each node. Therefore,
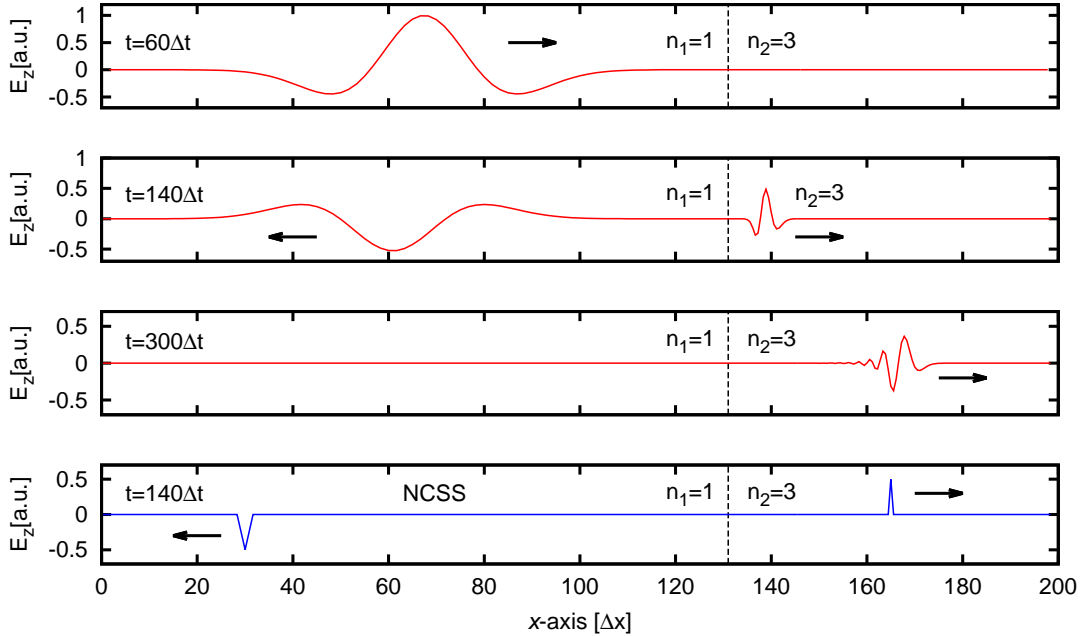

Figure 1.5: This set of figures compare numerical dispersion in one dimension. The Ricker pulse (second derivative of Gaussian) impacts the interface between free space on the left and dielectric on the right. In the first case, grid with constant spatial step Δ_x and $N_\lambda = 30$ is used. In the second case, the adaptive spatial step $\Delta_x(\varepsilon(x))$ is tested for $N_\lambda = 1$. Using the DFT we compute transmission coefficients which are compared in Fig. 1.6.
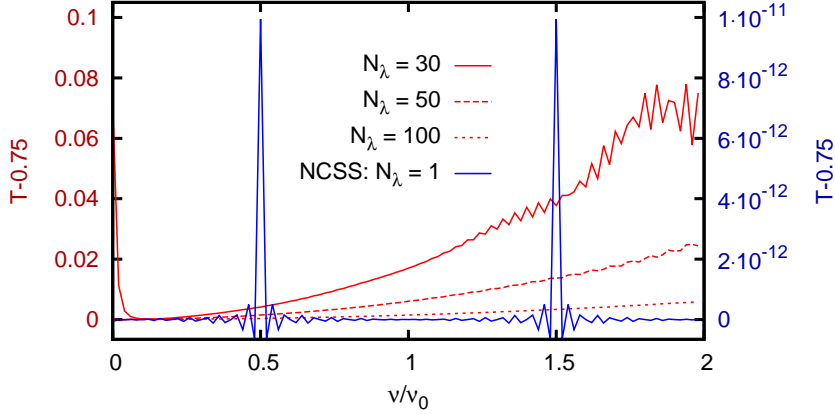
Figure 1.6: Comparison of transmission spectra for simple and adaptive spatial step Δ_x. Impact of numerical dispersion is clearly visible here. If $N_\lambda = 30$, non-physical results might be obtained. Nevertheless, in 1D might be the condition for the magic time-step fulfilled even in dielectrics. The transmission (blue) is not exactly 0.75 because of numerical errors of DFT.

the condition for the magic time-step $\Delta_x(x) = \Delta_{x_0}/n(x)$ is preserved even in dielectrics. The $n(x)$ is spatially dependant refractive index. As Fig. 1.5 illustrates, no numerical dispersion occurs although $N_\lambda = 1$!

The great force of magic time-step conservation shows Fig. 1.6, where the transmission spectrum of modelled interface is illustrated. Using the Fresnel equations we know, the transmission should be 0.75. We subtract $T(\nu) - 0.75$ to get curves shown in Fig. 1.6. Please note different y-axis scales. The transmission when non-constant spatial step is applied is non-zero only because of numerical errors of the DFT.

Unfortunately, the weakness of discussed method appears when numerous materials of particular thicknesses and refractive indices must be set into the grid.

Let's consider set several layers with thicknesses d_i and refractive indices n_i into the grid. The number of nodes in the grid, which represents the ith layer, is

$$X_i = \frac{d_i}{\Delta_x^i}, \qquad \text{where} \quad \Delta_x^i = \frac{c}{n_i}\Delta_t \qquad (1.20)$$

is the real distance of two points in the ith layer. The relationship which defines Δ_x^i ensures the existence of the magic time-step. Putting Δ_x^i to the first equation yields

$$X_i = \frac{n_i d_i}{c\Delta_t}. \qquad (1.21)$$

The fraction X_i/X_j therefore equals $n_i d_i/n_j d_j$. We can reformulate it into mathematical statement:

Find $\xi \geq 0$ so the expression $n_i d_i \xi/n_j d_j \xi$ is the fraction of two integers for all i, j. Then $X_i = n_i d_i \xi$ is also integer and 1D-FDTD provides exact numerical solution.

We will discuss this issue in Chap. 2.1.

20

1.3 Transfer Matrix Method

As mentioned in the introduction, FDTD is not the only one approach which can be used to solve electromagnetic problems. In some cases it is too robust and clumsy. Similar, or even better, results might be obtained in shorter computational time when different approach is used.

Transfer matrix method (TMM) is designed to calculate transmission or reflection coefficients (and also field distribution) of layered structures. Such structures are usually anti-reflective coatings and dielectric mirrors (one-dimensional PhCs). To explain how is the TMM working and what can we get from its formalism, we first take a look at the dielectric mirrors. Secondly, we compare TMM with 1D-FDTD simulation of an inhomogeneous dielectric slab. Finally, in Chap. 4, we investigate layered structure, which is similar to the holey waveguide, obtaining very good agreement although the structures and computational methods are different.

The idea of TMM is as follows: Denote the tangential components of electromagnetic field by E_{01}, H_{01} for the incident wave propagating in medium 0 close to the interface 0-1. Similarly, E_{12}, H_{12} denote components of the field close to the interface 1-2, propagating in medium 1. After the calculation, which is very similar to the derivation of Fresnel equations, we obtain following relation

$$\begin{pmatrix} E_{01} \\ \eta_0 H_{01} \end{pmatrix} = \begin{pmatrix} \cos\delta_1 & \frac{i\sin\delta_1}{\gamma_1} \\ i\gamma_1\sin\delta_1 & \cos\delta_1 \end{pmatrix} \begin{pmatrix} E_{12} \\ \eta_0 H_{12} \end{pmatrix}. \tag{1.22}$$

The matrix M for j^{th} layer of thickness d_j characterized by index n_j is therefore defined as

$$M = \begin{pmatrix} m_{11} & m_{12} \\ m_{21} & m_{22} \end{pmatrix} = \begin{pmatrix} \cos\delta_j & \frac{i\sin\delta_j}{\gamma_j} \\ i\gamma_j\sin\delta_j & \cos\delta_j \end{pmatrix}, \tag{1.23}$$

where

$$\delta_j = \frac{\omega n_j d_j}{c}\cos\alpha_j \tag{1.24}$$

and

$$\gamma_j = \frac{\cos\alpha_j}{Z_j} \qquad\qquad \text{for s-polarization,} \tag{1.25a}$$

$$\gamma_j = \frac{1}{\cos\alpha_j Z_j} \qquad\qquad \text{for p-polarization,} \tag{1.25b}$$

Z_j is the impedance and α_j is the angle of refraction (can be computed using the Snell's law).

For a structure composed of N layers, where each layer is described by its own matrix M_j, we get the following relation

$$\begin{pmatrix} E_{01} \\ \eta_0 H_{01} \end{pmatrix} = M_1 M_2 \dots M_N \begin{pmatrix} E_{N,N+1} \\ \eta_0 H_{N,N+1} \end{pmatrix}. \tag{1.26}$$

Finally, if we compute transfer matrix $M = M_1 M_2 \dots M_N$, we can easily obtain reflection and transmission coefficients

$$r = \frac{\gamma_0 m_{11} + \gamma_0 \gamma_t m_{12} - m_{21} - \gamma_t m_{22}}{\gamma_0 m_{11} + \gamma_0 \gamma_t m_{12} + m_{21} + \gamma_t m_{22}}, \tag{1.27}$$

$$t_\perp = \frac{2\gamma_0}{\gamma_0 m_{11} + \gamma_0 \gamma_t m_{12} + m_{21} + \gamma_t m_{22}}, \tag{1.28}$$

$$t_\parallel = \frac{Z_t}{Z_0} \frac{2\gamma_t}{\gamma_0 m_{11} + \gamma_0 \gamma_t m_{12} + m_{21} + \gamma_t m_{22}}. \tag{1.29}$$

1.3.1   Bragg mirror

In the previous sub-section we have defined all necessary theory and now we can calculate optical response of the dielectric mirror, also know as the Bragg mirror.

The typical Bragg mirror consists of a stack of thin dielectric layers of alternating refractive indices. The refractive index profile is illustrated in Fig. 1.7a. Incidence half-space is air. Alternating layers of SiO_2 ($n_L = 1.46$) and TiO_2 ($n_H = 2.4$) are deposited on the glass substrate, which fills half-space of transmittance. In order to produce constructive interference in the light reflected from the interfaces and destructive interference in the corresponding transmitted light,

Figure 1.7: The Bragg mirror composed of bilayers made of SiO_2 ($n_L = 1.46$) and TiO_2 ($n_H = 2.4$) deposited on the glass substrate ($n_s = 1.52$). (a) illustrates the refractive index profile and (b) compares the reflectance spectra for 4 and 10 bilayers computed using TMM formalism. As figure (b) indicates, for more bilayers we obtain broader region where $R \approx 1$. What will happen with spectrum when non-zero angle of incidence is considered, depicts Fig. 1.8. If we assumed theoretical mirror composed of infinite number of bilayers, we would get transmittance and reflectance spectra as Fig. 1.9 shows.
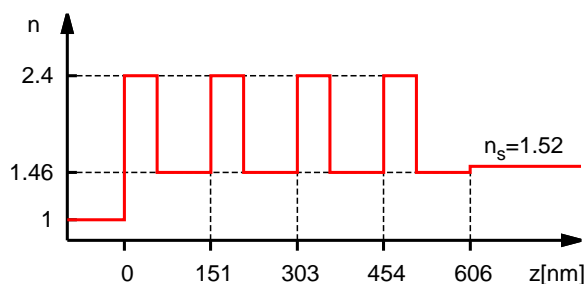
(a) Refractive index profile
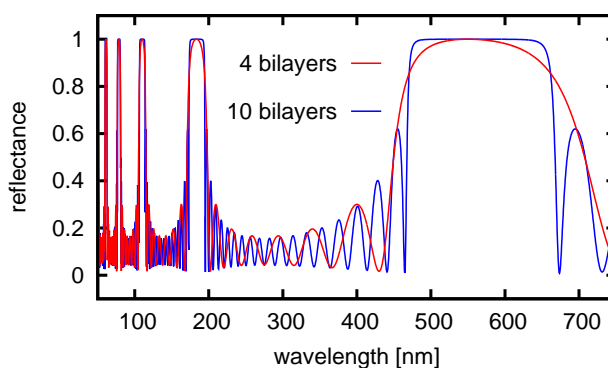
(b) Reflectance spectra

the optical thicknesses of layers are chosen as $\lambda_0/4$. Wavelength of interest is chosen as $\lambda_0 = 550$nm. The reflectance spectra for 4 and 10 bilayers are compared in Fig. 1.7b. The angle of incidence $\alpha = 0$.

As Fig. 1.7b indicates, the more bilayers we deposit on the glass substrate, the broader region where $T \approx 1$ we obtain. Coatings of current mirrors are often composed of several tens, or even hundreds of layers to achieve desired behaviour. Nevertheless, the optical sensitivity increases with the number of layers and even small manufacturing perturbations may completely destroy the mirror features [24].

When using mirrors in experiments, we may often require high reflectance for whole range of incident angles. Look at the Fig. 1.8 to see, what happens with the spectrum when non-zero angle of incidence α is present. High reflectance regions shift, and some wavelengths which were totally reflected for $\alpha = 0$ might pass trough without any losses ($\lambda = 650$nm, $\alpha \approx 33.5°$). When designing dielectric mirror, we are probably most interested in regions where $R \approx 1$ for all incident angles α.
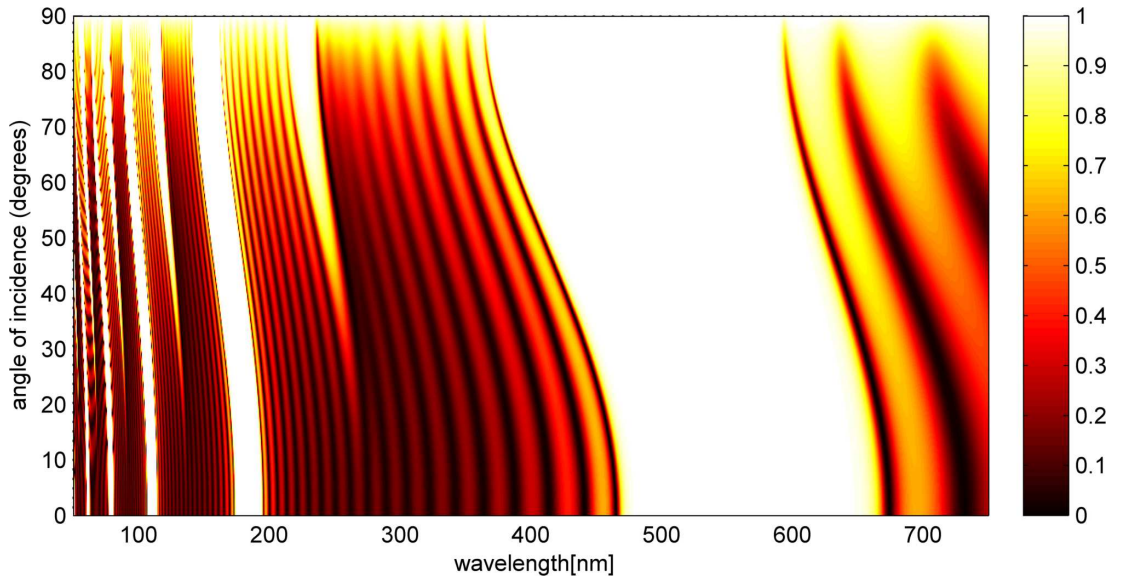

Figure 1.8: The dependence of the reflectance spectrum of the Bragg mirror with ten bilayers (see Fig. 1.7b) on the angle of incidence α. For $\alpha \approx 90°$ we get $R = 1$ for all wavelengths. Please note, that for all wavelengths between $\sim(480$–$590)$nm the mirror perfectly reflects at all angles of incidence. This is very useful when designing a mirrors. The s-polarized light was assumed when calculating this figure.

1.3.2   Infinite Bragg mirror

We restrict ourselves to a theoretical considerations for a while, and investigate what happens when the mirror is composed of infinite number of layers.

For the sake of simplicity, we assign alpha to zero. Since the optical thicknesses $n_j d_j$ of both layers are $\lambda_0/4$, the $\delta_j = \pi/2$. Therefore, according to (1.23), the transfer matrix of bilayer is

$$M_{\text{bl}} = \begin{pmatrix} 0 & \frac{i}{\gamma_H} \\ i\gamma_H & 0 \end{pmatrix} \begin{pmatrix} 0 & \frac{i}{\gamma_L} \\ i\gamma_L & 0 \end{pmatrix} = \begin{pmatrix} -\frac{n_L}{n_H} & 0 \\ 0 & \frac{n_H}{n_L} \end{pmatrix}, \tag{1.30}$$

where indices L and H stands for low and high refractive index. For a mirror composed of N bilayers we have to calculate the Nth power of the matrix M_{bl}. Since the matrix is diagonal, the exponentiation is very easy

$$M = M_{\text{bl}}^N = \begin{pmatrix} -\frac{n_L}{n_H} & 0 \\ 0 & \frac{n_H}{n_L} \end{pmatrix}^N = \begin{pmatrix} (-n_L/n_H)^N & 0 \\ 0 & (n_H/n_L)^N \end{pmatrix}. \tag{1.31}$$

Finally, using (1.27) we can evaluate the reflection coefficient r and reflectivity R

$$r = \frac{\left(-\frac{n_L}{n_H}\right)^N - n_s \left(-\frac{n_H}{n_L}\right)^N}{\left(-\frac{n_L}{n_H}\right)^N + n_s \left(-\frac{n_H}{n_L}\right)^N}, \tag{1.32}$$

$$R = \left[\frac{\frac{1}{n_s}\left(\frac{n_L}{n_H}\right)^{2N} - 1}{\frac{1}{n_s}\left(\frac{n_L}{n_H}\right)^{2N} + 1} \right]^2. \tag{1.33}$$

It is obvious, that $R \xrightarrow{N\to\infty} 1$. Nevertheless, it is important to notice that the result was calculated just for wavelength $\lambda_0 = 550\text{nm}$. Our goal is to compute R for all wavelengths.

For $\lambda \neq \lambda_0$ the condition $\delta_j = \pi/2$ is not longer valid. Thus also the matrix M_{bl} is not diagonal. It leads us to linear algebra and eigensystem. Using the eigenvalues and eigenvectors we find the basis in which M_{bl} is diagonal. Then, the power M_{bl}^N can be done easily. Unfortunately, the result $\lim_{N\to\infty} M_{\text{bl}}^N(\lambda)$ diverge in many cases and therefore we cannot evaluate r. We can deal with this problem as follows:

$$r_{\text{final}}(\lambda) = \lim_{N\to\infty} r\left(M_{\text{bl}}^N(\lambda)\right). \tag{1.34}$$

To summarize, firstly we find eigensystem of M_{bl}, secondly we power the matrix to a general power N, then we compute reflection coefficient r, which depends on N, from elements of matrix M_{bl}^N and finally we compute the limit (1.34). Since the infinity is not computer-size number for most programs, we used *Mathematica* software tool which can deal with it. The limit (1.34) does not converge for every wavelength. It may also oscillate or even diverge in some special cases. The result of our effort is demonstrated in Fig. 1.9.

As can be seen, the limit oscillates quite often. Therefore, we plotted maxima and minima and coloured the area between. This area corresponds to all possible solutions. The regions where $R < 0$ (or $T > 1$) are non-physical. In these cases the formalism of TMM fails, since it is not design for infinite space as well as not for very thick layers. To ensure the result is correct, we can see the regions where $R = 1$ correspond to Fig. 1.7b nicely.
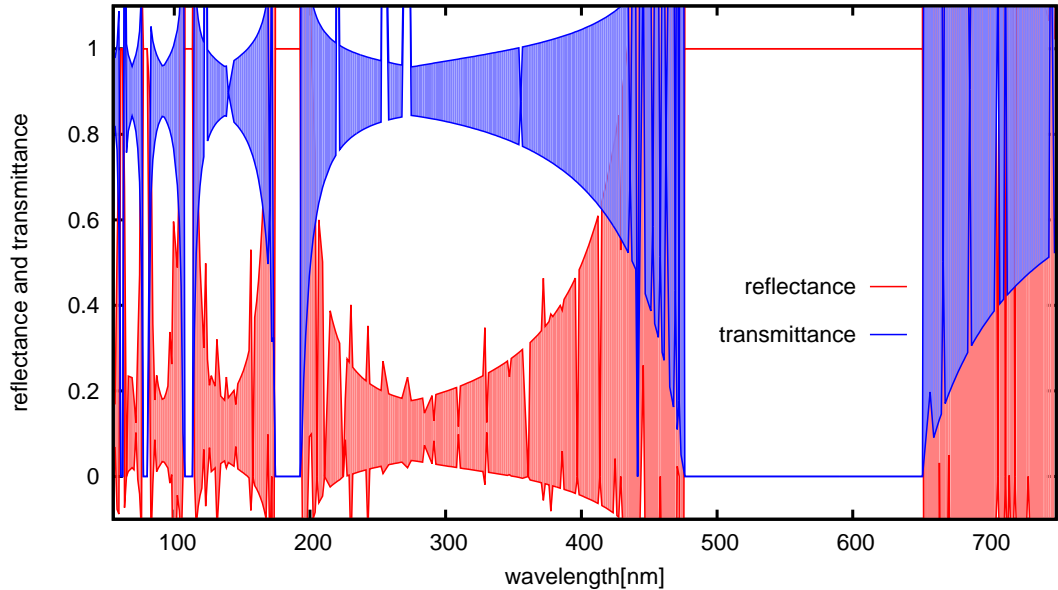
Figure 1.9: Thought experiment where infinite number of bilayers is assumed. The limit (1.34) converges only for wavelengths in bang gaps. We plot maximum and minimum of R (T) and colour the area between for all wavelengths where the limit oscillates. It means, the solution can lie anywhere in filled area.

1.3.3 Dispersion relations

The photonic crystals do not have to be some extra special structures. As shown above, even the Bragg mirror composed of many layers exhibits such a phenomenon as band gaps. It is simply one-dimensional PhC. We know PhCs have band structure and band gaps. To show it analytically we can start with Maxwell's equations, construct operators, and similarly as in quantum mechanics compute dispersion relations which appears due to periodical permittivity (see [1] for more details). Instead of this long procedure we show here, how can be dispersion relations obtained from introduced transfer matrix formalism.

We consider a medium with permittivity, which is homogeneous in xy-planes and periodical in z direction. The period is $\Lambda = d_1 + d_2$, where $d_{1,2}$ are thicknesses of two alternating layers with refractive indices $n_{1,2}$. The permittivity is therefore defined as

$$\varepsilon(z) = \begin{cases} \varepsilon_1 & \text{for} \quad n\Lambda < z < n\Lambda + d_1 \\ \varepsilon_2 & \text{for} \quad n\Lambda + d_1 < z < (n+1)\Lambda \end{cases} \quad ; \quad \varepsilon(z) = \varepsilon(z + \Lambda). \tag{1.35}$$

When calculating dispersions relations in crystals, we describe a particle propagating through a periodical potential by a periodical wave function using the Bloch theorem[4]. This theorem is applicable also in electromagnetic theory. It states, the electromagnetic field is periodical due to periodical permittivity [25]

$$E_K(x, y, z) = E_K(z)e^{-iKz}e^{-i(k_x x + k_y y)}, \tag{1.36}$$

---

[4]The theorem was postulated independently several times and is also known as Floquet's theorem.

where $E_K(z) = E_K(z + \Lambda)$ is periodical function and K is known as the Bloch wave number. Using the notation we defined in the beginning of TMM, we can state (do not confuse quantum number K with interface index N)

$$E_{N,N+1}(z) = E_{N-1,N}(z + \Lambda) = e^{-iK\Lambda}E_{N-1,N}(z). \tag{1.37}$$

We used the periodicity of electric field first, and then Bloch's theorem. When applying Bloch's theorem also on magnetic intensity, using (1.26), and moving imaginary exponential to the other side in (1.37), we can write

$$\begin{pmatrix} m_{11} & m_{12} \\ m_{21} & m_{22} \end{pmatrix} \begin{pmatrix} E_{N,N+1}(z) \\ H_{N,N+1}(z) \end{pmatrix} = \begin{pmatrix} E_{N-1,N}(z) \\ H_{N-1,N}(z) \end{pmatrix} = e^{iK\Lambda} \begin{pmatrix} E_{N,N+1}(z) \\ H_{N,N+1}(z) \end{pmatrix}. \tag{1.38}$$

First and third part of the relation give us an eigenproblem. The $e^{iK\Lambda}$ is the eigenvalue of the transfer matrix M. Solving this problem we have to deal with quadratic equation. According to the definition of M (1.23) we know $m_{11}m_{22} - m12m_{21} = 1$ and $\frac{1}{4}(m_{11} + m_{22})^2 \leq 1$. This gives us finally the dispersion relations

$$\cos(K\Lambda) = \frac{1}{2}(m_{11} + m_{22}). \tag{1.39}$$

The dispersion relations (1.39) are shown in Fig. 1.10 for the same parameters as used to describe Bragg mirror. Wide photonic band gap appears between
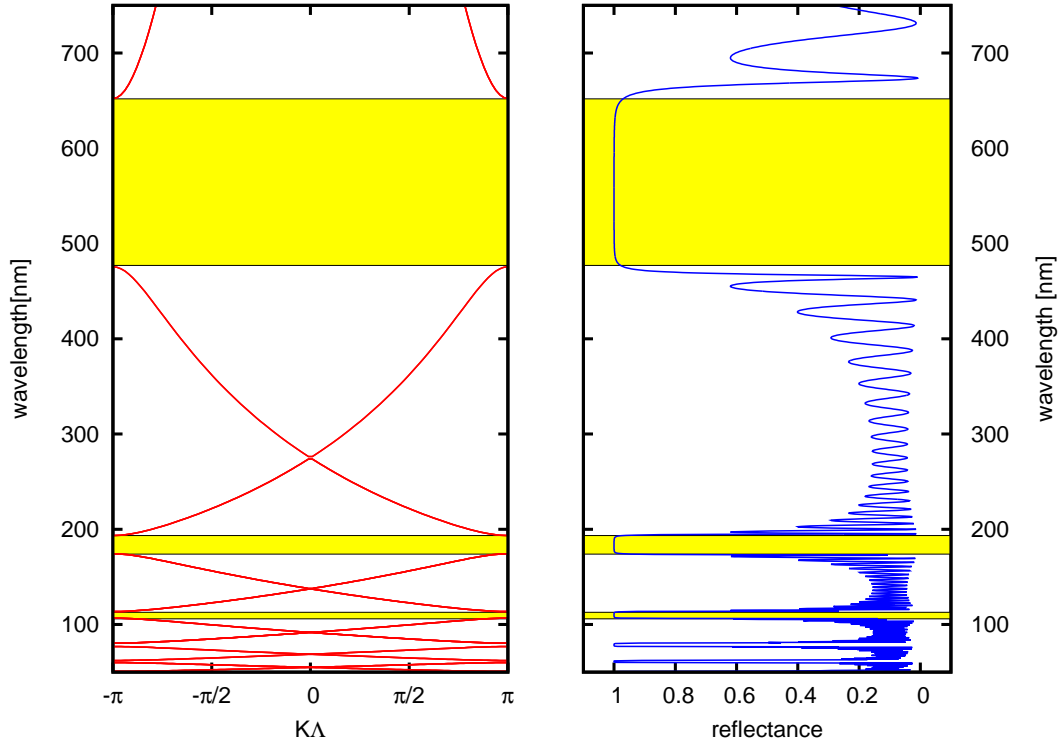

Figure 1.10: Dispersion relations (1.39) computed for parameters of the Bragg mirror as illustrated in Fig. 1.7a. Band gaps are compared here with reflectance spectrum of Bragg mirror with 10 bilayers. Band gaps, which appear here, are in absolute agreement with band gaps which can be read from Fig. 1.9.

470–650nm and many others are visible at lower wavelengths. Band gaps shown in Fig. 1.9 and Fig. 1.10 are in absolute agreement.

For this simple one-dimensional case the derivation of dispersion relations was not too hard. If we would like to investigate optical properties of more complicated structures like three dimensional PhC made of spheres, we would need to satisfy ourself only with a numerical solution. Nevertheless, even some special 3D cases can be partially solved analytically [26].

2. Verification of the FDTD code

In previous chapter we introduced FDTD algorithm, described its advantages and weaknesses and formulated TMM. To be sure our code does produce reasonable results, we are going to test it on various simple structures where the analytical solution exists or where it can be compared with other numerical approaches.

For illustrative purposes, we start with the simplest case — one dimensional problem.

2.1 Inhomogeneous dielectric step

In this section we compare FDTD with TMM. Since we use grid with non-constant spatial step, we can expect the results should be very similar.

We consider an inhomogeneous dielectric step which illustrates Fig. 2.1. The half-space of incidence is filled with air ($n_1 = 1$) and the half-space of transmittance is filled with material of refractive index $n_2 = 4$. The interface between free space and material is not a step but refractive index varies linearly from n_1 to n_2 at distance L.

If L is zero, we will use Fresnel equations and evaluate reflection coefficient as $R = 0.36$. But since $L \geq 0$, the situation is not so clear.
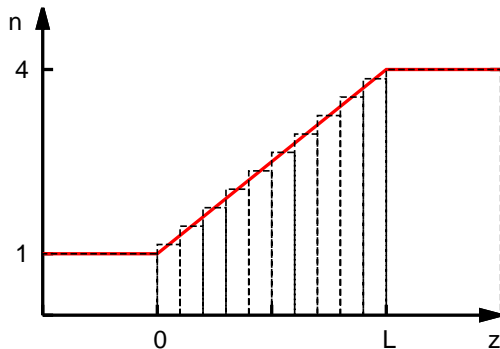
Figure 2.1: Refractive index profile of inhomogeneous dielectric slab. The continuous function (red line) is approximated by staircase profile (dashed black line). For better readability, the number of layers N illustrated here is only 10. In simulations we use $N = 100$. The incident light propagates in free space and then impacts the inhomogeneity.

We use staircase approximation for refractive index profile to model this continuous structure. In TMM language it means, we define $N = 100$ layers of uniform thicknesses $d = L/N$ with varying refractive indices and stack them one on the other. This is denoted in Fig. 2.1 by dashed lines. In FDTD, the numbers in permittivity array change analogically.

The reflectance spectra are compared Fig. 2.2. We first describe the profile of general reflectance spectrum as shown in the inset. It is intuitive, that for $L \ll \lambda$, the incoming wave will feel something like a simple step rather than continuous change and reflects like from an ordinary interface. But if $L \gg \lambda$, the wave will not feel any significant changes of the refractive index and passes completely through. The last region, where $L \approx \lambda$, corresponds to Fabry–Pérot-like interferometer. The wave partially oscillates inside the slab, which is the analogy of reflectance of planparallel desk.

As we mentioned above (in Sec. 1.2.3), we can get an exact numerical solution with one-dimensional FDTD when we use the magic time-step. That can be
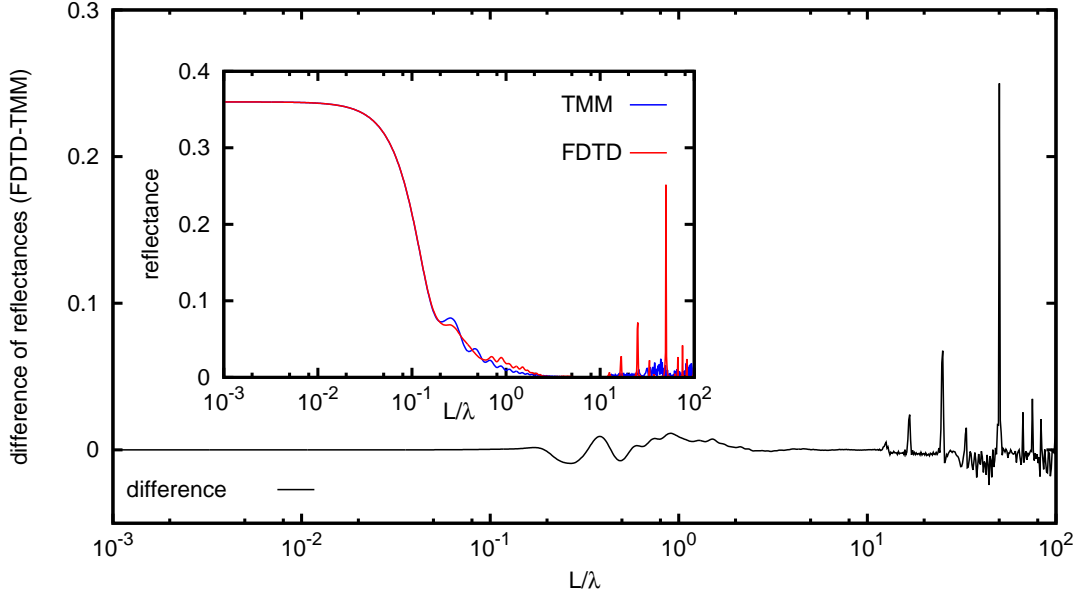
Figure 2.2: The comparison of reflectance spectra of the inhomogeneous dielectric slab obtained from TMM and FDTD. The profile of spectrum in the inset corresponds more or less to the intuitive idea, where very long wavelengths feel a simple step, whereas extremely short wavelengths do not feel almost any significant change of RI. The difference of reflectance spectra illustrates weakness of non-constant spatial step in 1D-FDTD and not ideal approximation of continuous change of RI.

achieved even in dielectric materials if non-constant spatial step is used. The question is, why Fig. 2.2 shows non-zero difference between FDTD and TMM? The error is not in TMM but really in FDTD.

Definition of layers in TMM is very simple since the input parameters are only thickness and refractive index of the particular layer. In FDTD we must be much more careful.

At the end of Sec. 1.2.3 we formulated the way, in which the resolution must be defined to obtain exact results of multilayered models. In this case ($N = 100$, $n_1 = 1$, $n_2 = 4$) we unfortunately find out, the inhomogeneous interface should be modelled with very large number of grid points (24750). To get results in real time, we reduce this number and get imperfect result due to incorrect layer thicknesses. Since the limits $L \ll \lambda$ and $L \gg \lambda$ should be correct even in this approximation, we get the biggest difference for $L \approx \lambda$.

The noise in the very right area of the reflectance spectrum (in Fig. 2.2) corresponds to oscillations in particular layers. If $N \gg 100$, the numerical noise will disappear.

After analysing inhomogeneous dielectric slab we can shamelessly say the TMM is more powerful approach than FDTD in the case of one-dimensional structures. Nevertheless, simple TMM method, as formulated here, cannot be applied to higher dimensions. We will use TMM once again in Sec. 4.1, where we will investigate behaviour of resonance peak in holey waveguide-like structure.

2.2 Gaussian beam

The excitation of the incident light into the Yee grid can be done in many, many ways. In the simplest case we can excite only one node (i.e. $E_z^q[m,n] = f(q)$, where $f(q)$ is an arbitrary time-dependent excitation function), which leads to the point source with spherical wavefronts. If we want to simulate propagation of plane waves, we will have to use a little bit more complex method called TFSF described in Sec. 1.2.2.

Besides the spherical and plane waves we can, of course, simulate any arbitrary pulse or whatever we want (e.g. Gaussian beam modulated in time with a Gaussian pulse).

The shape of Gaussian beam (spatial distribution) can be obtained by precise excitation of several nodes which lie in the line, whereas the Gaussian pulse is provided by time-dependent function $f(q)$ as mentioned above. It is very useful to demonstrate, how is the focused laser beam diffracted on a grating, or to demonstrate interaction of a pulsed Gaussian beam with a gainy medium [27].

We remind parameters of Gaussian beam now. If the light propagates along the z-axis, the electric field is described as [28]:

$$E(r,z) = E_0 \frac{w_0}{w(z)} e^{-\frac{r^2}{w^2(z)} - ik\left(z - \frac{r^2}{2R(z)}\right) + i\zeta(z)} e^{i\omega t}, \qquad \text{where} \qquad (2.1a)$$

$$E_0 = |E(0,0)| \qquad \text{is the maximum amplitude,}$$

$$r = \sqrt{x^2 + y^2} \qquad \text{is the radial distance from the axis of the beam,}$$

$$w(z) = w_0 \sqrt{1 + \left(\frac{z}{z_R}\right)^2} \qquad \text{is the radius at which the amplitude drops to } \frac{1}{e},$$

$$w_0 = w(0) \qquad \text{is the waist size,}$$

$$z_R = \frac{\pi w_0^2}{\lambda} \qquad \text{is the Rayleigh distance,}$$

$$R(z) = z\left[1 + \left(\frac{z_R}{z}\right)^2\right] \qquad \text{is the radius of curvature of the wavefronts,}$$

$$\zeta(z) = \arctan\frac{z}{z_R} \qquad \text{is the Gouy phase shift.}$$

If we compute $E(r,z)$ everywhere in the two-dimensional space, we will obtain field distribution as shown in Fig. 2.3. The figure depicts Gaussian beam which has $w_0 = 1.5\lambda$, where λ is an arbitrary wavelength. Diagonal (source) line indicates, where is the field computed in FDTD simulation. Changing the angle θ we can easily excite Gaussian beam at different angles using just one row of nodes in the Yee grid.

What happens if such beam hits a grating? It diffracts, as we know. After some straightforward calculations we can derive so-called grating equation, which describes diffracted angle maxima [29]:

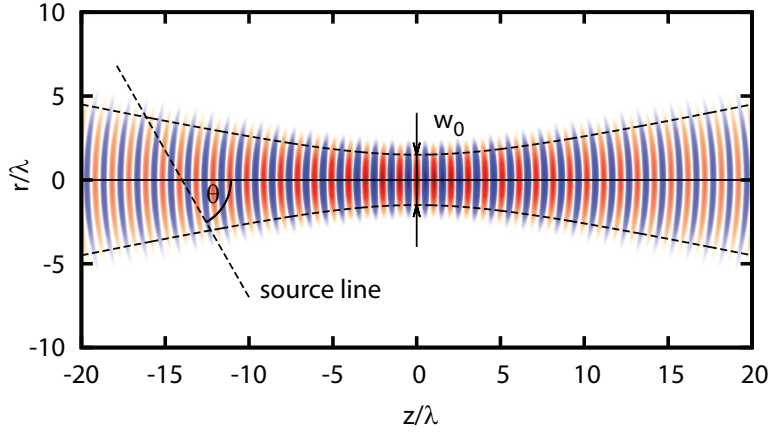$$d(\sin\theta_i + \sin\theta_m) = m\lambda, \qquad (2.2)$$

Figure 2.3: Using the equation for Gaussian beam (2.1a) we can easily compute the spatial distribution of the electric field. The waist size is $w_0 = 1.5\lambda$. The source line corresponds to the source line in Fig. 2.4, where E_z is calculated in FDTD simulation.

where d is the grating period, θ_i is the angle of incidence, θ_m are the angles at which the diffracted light will have maxima, m indicates order of particular maximum and λ is wavelength of incident light.

Figure 2.4 depicts time-integrated intensity of the Gaussian beam which impacts the grating. Grating period is $d = 1.5\lambda$, height of pitch is 0.2λ and angle of incidence $\theta_i = 60°$. Putting these parameters into the grating equation (2.2) we obtain three diffracted maxima $\theta_m = -60°, -11.5°, 27.9°$ for $m =$ 0,1,2. These angles are designated by broken lines. According to the results we can say, the two-dimensional FDTD works correctly (meaning that the propagation of fields is reasonable). Using FDTD simulation we calculate only the near-field. Nevertheless, in experiments we are more interested in things which can be observed in the far-field, i.e., far away from grating compared to light wavelength. The near-to-far-field transformation can be done in FDTD using a bit more complicated analysis of diffracted light. As a result we would obtain radiated intensity for each angle [13, Chap.9].

Using this technique we can investigate the field decomposition nearby a grating as well as diffracted angle maxima when computing just one single simulation. Some different and more complicated grating profiles (sinus, blazed) can be assumed.

To obtain results as shown in Fig. 2.4 we used grid of sizes 1100×700 nodes and 20 points per wavelength.

If we would like to do an experimet, we could use DVD (the track pitch is 740nm) as the grating and laser with $\lambda = 493$nm as incident light. If we would tilt DVD at the angle of 60°, we should see these three different diffracted angle maxima computed above.
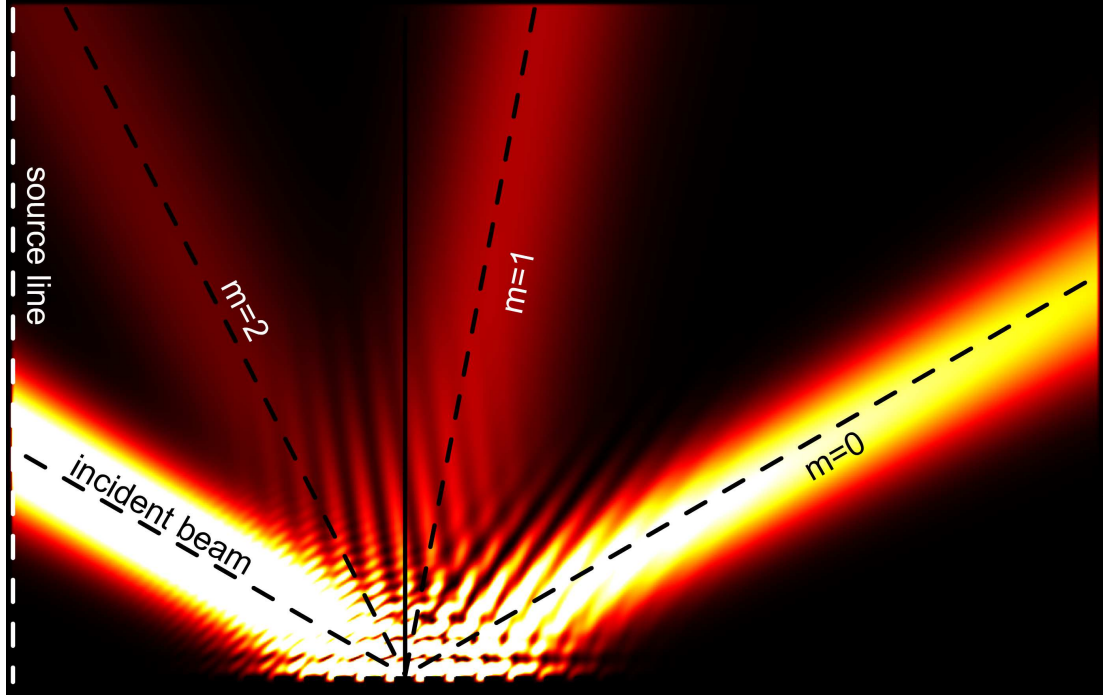
Figure 2.4: Time-integrated intensity of the Gaussian beam which is excited at the source line (as is illustrated in Fig. 2.3) and at the angle of 60° impacts the grating. The beam is focused on the grating surface where single pitches can be seen. Grating period is 1.5λ, height of pitch is 0.2λ. Considering grating equation (2.2) we obtain angles -60°, -11.5° and 27.9° for m=0,1,2. These three maxima are designated by the broken lines.

2.3 Waveguide modes

As mentioned in the introduction, integrated optics and waveguides are currently being used worldwide and provide us very fast communication. To show that behind the data transfer via waveguides is something more than light bulb flickering, we examine here eigenmodes of a plane symmetrical waveguide.

We consider here the symmetrical plane waveguide which is made of material parameters ε_1, μ_1 and thickness d. Waveguide lies in yz-plane and is perpendicular to x-axis. Surrounding of the waveguide is characterized by parameters ε_2 and μ_2. In next paragraph, we look for even transverse magnetic (TM) modes (E_x, H_y, E_z), which are propagating along the z-axis.

Maxwell's equations (1.5) together with assumption that the electromagnetic field is harmonic inside the waveguide and exponentially attenuated outside lead to following formulae [30, 31]:

$$E_x^{(1)} = \frac{\beta}{\omega \varepsilon_1} A_e \cos(\kappa x) \qquad E_x^{(2)} = \frac{\beta}{\omega \varepsilon_2} A_e \cos(\kappa d) e^{-\gamma(|x|-d)}, \qquad (2.3a)$$

$$H_y^{(1)} = A_e \cos(\kappa x) \qquad H_y^{(2)} = A_e \cos(\kappa d) e^{-\gamma(|x|-d)}, \qquad (2.3b)$$

$$E_z^{(1)} = i \frac{\kappa}{\omega \varepsilon_1} A_e \sin(\kappa x) \qquad E_z^{(2)} = i \frac{x}{|x|} \frac{\beta}{\omega \varepsilon_2} A_e \cos(\kappa d) e^{-\gamma(|x|-d)}, \qquad (2.3c)$$

where A_e is an amplitude, ω is an angular frequency, $\kappa = \sqrt{\omega^2 \varepsilon_1 \mu_1 - \beta^2}$, $\gamma = \sqrt{\beta^2 - \omega^2 \varepsilon_2 \mu 2}$ and $\beta = N\frac{\omega}{c} = k_z$ is a propagation constant of the guided wave. Effective refractive index is given by $N = n_1 \sin\theta$, where θ is the incident angle under which the light impacts waveguide interfaces. Furthermore, if we assume that the tangential field components E_x and H_y must be continuous at the interfaces (i.e. $H_y^{(1)}(\pm d) = H_y^{(2)}(\pm d)$ and $E_z^{(1)}(\pm d) = E_z^{(2)}(\pm d)$), we obtain so-called *characteristic equation* for TM modes in symmetrical waveguide

$$\tan \kappa d = \frac{\varepsilon_1}{\varepsilon_2} \frac{\gamma}{\kappa} \qquad \text{for even modes,} \qquad (2.4a)$$

$$\tan \kappa d = -\frac{\varepsilon_2}{\varepsilon_1} \frac{\kappa}{\gamma} \qquad \text{for odd modes.} \qquad (2.4b)$$

These equations must be considered when waveguides are designed. Analytical solution is not available, therefore we solve it numerically. Equations (2.4a) are plotted in Fig. 2.5 for different wavelengths propagating in the same waveguide of thickness d. Intersections designated by dots mark all correct solutions. For
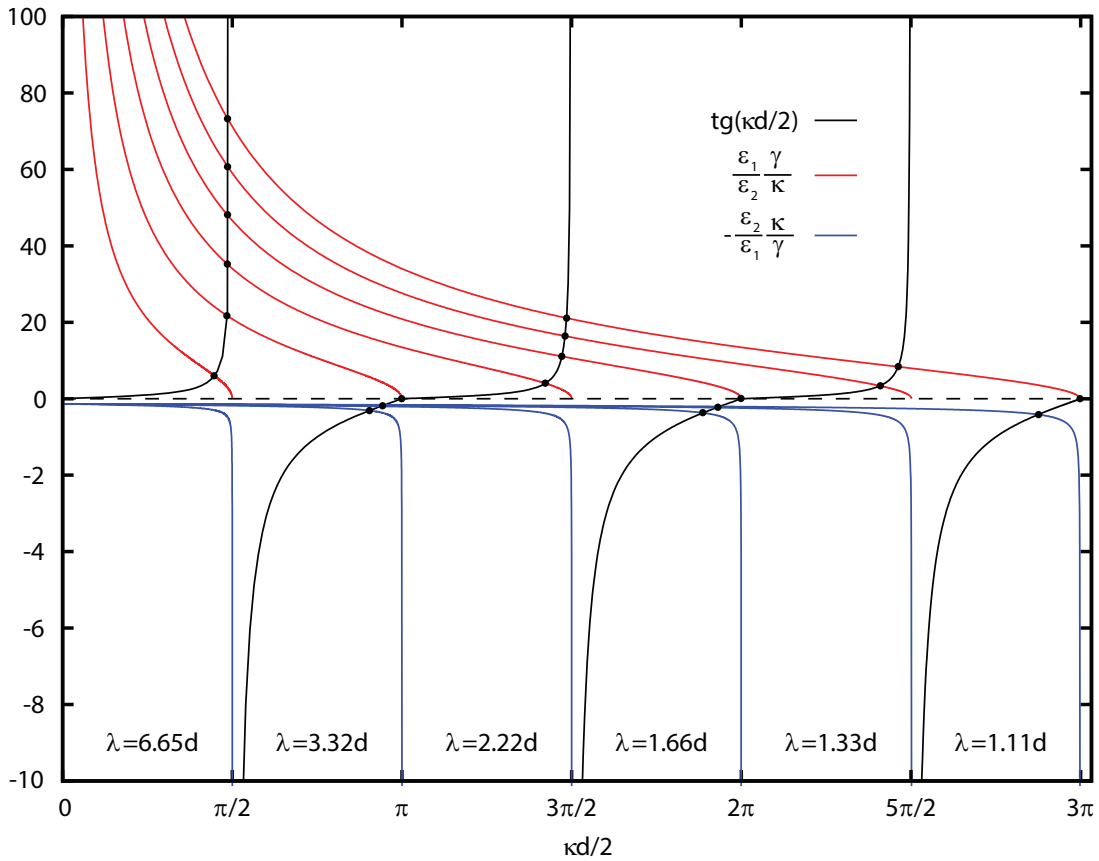

Figure 2.5: Graphical solution of characteristic equation for TM modes in symmetrical waveguide (Eq. (2.4a)) made of silicon ($n_1 = \sqrt{\varepsilon_1} = 3.47$). Red (blue) lines designate even (odd) modes. Intersections with black tangents are the solutions. For $\lambda \geq 6.65d$, we have one solution and the waveguide is single-mode. For $6.65d \leq \lambda \geq 3.32d$, we get one even and one odd guided mode. For better readability the negative part of the figure is stretched more than the positive part.

wavelengths greater than $\lambda = 6.65d$ we have only one available solution, which means the waveguide allows propagation of only one mode — it is single-mode waveguide. Theoretically, the waveguide can guide light of any arbitrarily small frequency. We say, the cut-off frequency is zero. If we decrease wavelength (increase frequency), we will obtain more solutions and the waveguide is called multi-mode.

We choose $\lambda = 3.33d$. According to characteristic equation (2.4a) we get one even and one odd mode. Since we know κd from numerical solution, we can compute spatial distribution of E_x, H_y and E_z from Eq. (2.3a)[(1)]. The field components are depicted in Fig. (2.6).

(a) E_x, even mode.   (b) H_y, even mode.   (c) E_z, even mode.

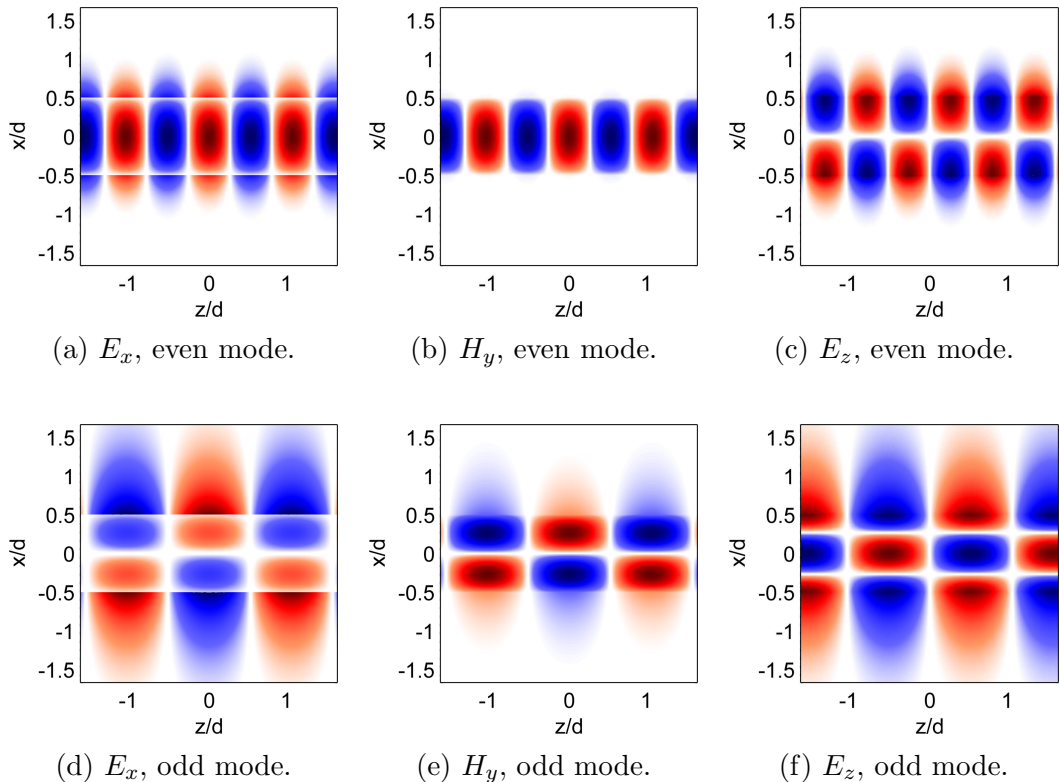(d) E_x, odd mode.   (e) H_y, odd mode.   (f) E_z, odd mode.

Figure 2.6: Field distribution of even and odd eigenmodes, which can propagate in planar symmetrical waveguide (TM polarization). The thickness of the waveguide is d and the wavelength of light is $\lambda = 3.33d$. No other modes can propagate under considered conditions.

Implementing eigenmodes to FDTD simulation is quite similar as exciting the Gaussian pulse in previous case. We have to define thickness d, wavelength λ, and using Eq. (2.3a) we excite the eigenmode to the Yee grid. We will discuss this issue later in Chap. 4, where we will investigate behaviour of the holey waveguide.

Similar analytical description, as partially expressed here, is also possible for asymmetric plane waveguides (very similar), optical fibres with radial symmetry (Bessel functions), hollow metallic waveguides, and some other special cases. In Sec. 4.3 we will design silicon rectangular waveguide on SiO_2 wafer. Unfortu-

---

[1]When solving characteristic equation (2.4a), we do not look for κ but for effective refractive index N. When we know N, we can express κ as well as γ very easily.

nately, for dielectric waveguides of rectangular cross section any exact analytic solution does not exist [32] and approximation techniques must be used [33].

2.4   3D diffraction

We do not want to settle only with at two dimensional cases but also move forward to the more realistic third dimension. One of the simplest three dimensional structures is certainly light diffraction on a circular aperture.
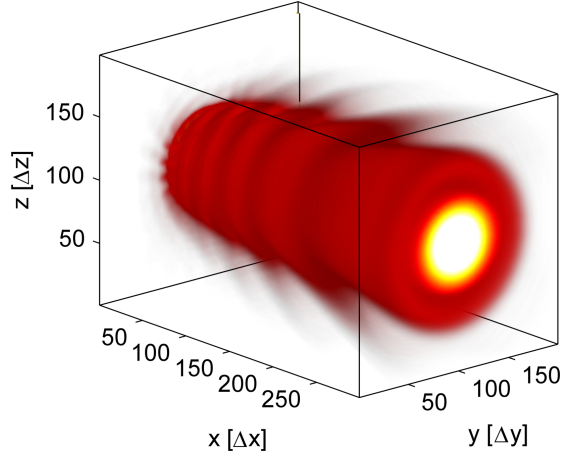

Figure 2.7: Time-integrated intensity of a plane wave which propagates in x-direction and diffracts on a metallic plate with the circular aperture. Diameter of the aperture is $d = 8\lambda$. Points per wavelength N_λ=10, grid dimensions: 300×200×200.

We consider a plane wave which impacts metallic plate with the circular aperture. Time-integrated intensity of such simulation is depicted in Fig. 2.7. Cross-section of electric field is shown in Fig. 2.8.

Analytical solution which describes the near-field could be hardly expressed. Using some approximations, we can compute diffracted angle maxima for the far-field where the Airy disc could be detected. Since near-to-far-field transformation is no implemented, we have to use some another approach to describe the near-field right behind the aperture.

The Fresnel diffraction (FD) integral, which is an approximation of Kirchhoff-Fresnel diffraction integral and describes waves in the near field, is defined as [34]
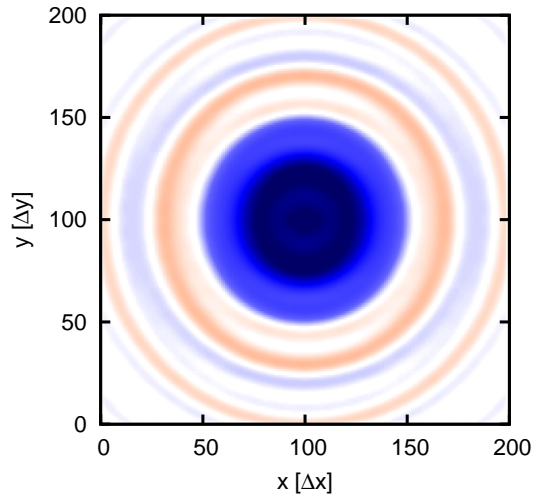

Figure 2.8: E_y at a distance of 12.6λ behind the circular aperture computed with FDTD. Diameter of the aperture is $d = 8\lambda$. Since the polarized light was used, slight radial asymmetry is present. The horizontal cross-sections of the electric fields in the middle ($E_y(x, 100\Delta_y, 126\Delta_z)$) obtained from FDTD and FD are compared in Fig. 2.9.

36

$$E(x, y, z) = \frac{z}{i\lambda} \int\limits_{-\infty}^{+\infty}\!\!\!\int \frac{E(x', y', 0)}{r^2} e^{ikr} \mathrm{d}x' \mathrm{d}y', \qquad (2.5)$$

where $E(x', y', 0)$ is the aperture and $r = \sqrt{(x - x')^2 + (y - y')^2 + z^2}$. Analytical solution of the integral (2.5) is known for few simplest geometries. Therefore, we will use only numerical description.

Using the Fresnel propagation we can calculate field $E(x, y, z_0)$, where $z_0 = 12.6\lambda$ is the distance from aperture to the shade or detector. Using FDTD we compute three-dimensional field behind the aperture. If we calculate cross-section at some distance z_0, we get two dimensional field as Fig. 2.8 illustrates. If we select horizontal cross-section in the middle of this two-dimensional field, we will get one-dimensional dependence of electric field upon the x-axis. This result is compared in the Fig. 2.9 with FD.

Small differences (max.10%) could be attributed to the small resolution used in FDTD (N_λ=10). Due to such small resolution we get large numerical dispersion, which leads to inexact results. When using FD (2.5) we do not consider polarized light, which is used in FDTD. Involving all these aspects we can say, we achieved reasonable agreement between FDTD and FD.
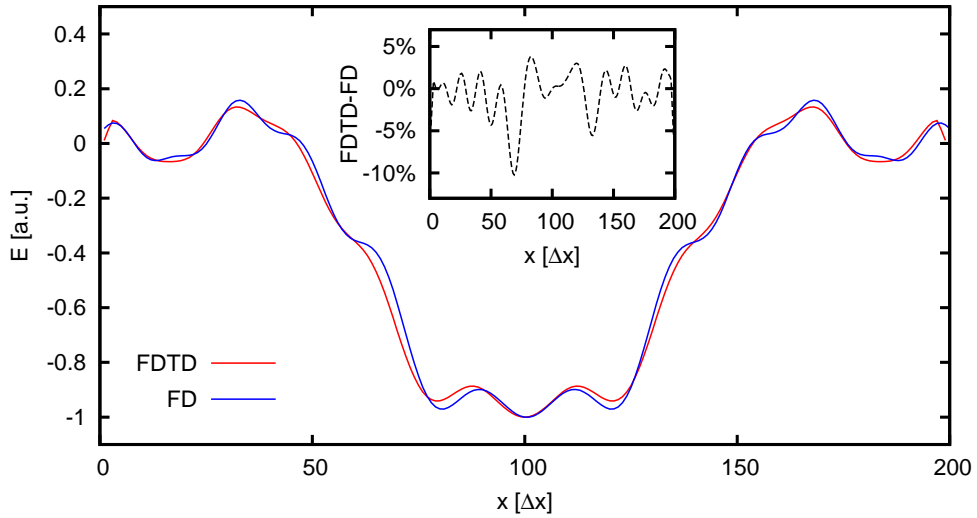

Figure 2.9: Comparison of results from FDTD simulation and Fresnel diffraction. Figure compares the cross-sections of the electric field profiles at a distance of 12.6λ behind the circular aperture. The inset demonstrates the result of subtraction, i.e. FDTD-FD.

3. Photonic crystals

With respect to the motivation of this thesis we focus on following structures, which might be interesting for biosensing applications. In this chapter we propose two-dimensional photonic crystals for enhanced sensitivity of biosensing devices. In the next chapter we will continue even to three-dimensional simulation of photonic structure known as holey waveguide.

The photonic nanostructures we propose here are designed for enhanced sensitivity of biosensing devices. These structures are usually made of silicon on insulator buffer (SiO_2) with refractive indices $n_{Si} = 3.47$ and $n_{SiO_2} = 1.44$. We tune these structures at $\lambda = 1550$nm due to waveguide compatibility[1]. The main features of investigated structures are the significant changes in optical response upon the presence of investigated medium. We can detect either the position band of the gap edge (cut-off wavelength) or position of some resonant peak inside the band gap. Figure 3.1 shows dispersion relations of a PhC with hexagonal lattice. As can be seen, even small variation of refractive index significantly changes optical band structure. More theory about resonant peaks is described in Sec. 4.1.
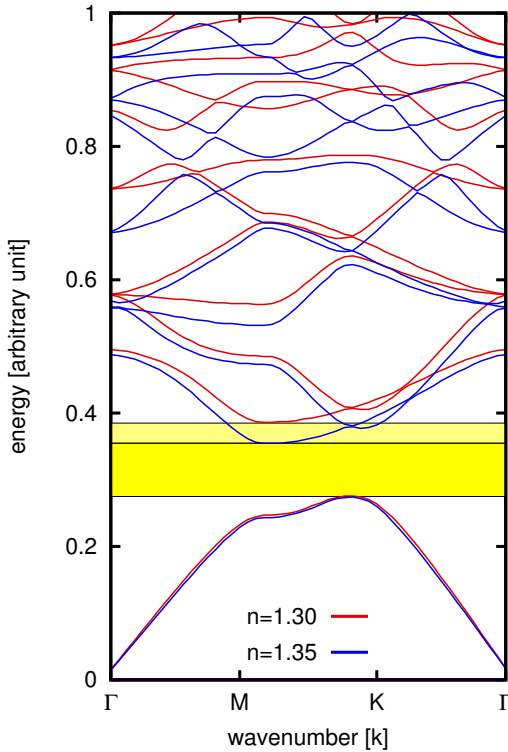

Figure 3.1: Dispersion relations of a two-dimensional hexagonal PhC (TE^z polarization). Band gap is clearly visible here. As refractive index of applied medium changes, significant shift of the band gap edge could be detected. The bigger shift of the edge is detected, the better sensitivity (shift of the edge in nanometres per refractive index unit) we get. The y-axes represents energy (i.e. frequency) and not wavelength as in Fig. 1.10. Therefore, the continuum of bands appears at the top and not at the bottom. Letters Γ, K and M represent different points in the first Brillouin zone.

Two main properties we analyse here are the sensitivity S and quality Q.

The sensitivity is measured in nanometres per refractive index unit (nm/RIU). It tells us, how many nanometres will the peak position or band gap edge shift if the refractive index of investigated medium will change by one. In this and next

---

[1]It means that edge of band gap or resonant peak is at position about 1550nm.

chapter we compute sensitivity from two spectra when refractive index of sensed medium is 1.3 and 1.35.

The peak quality, or just Q-factor, represents the width of a resonant peak. The greater Q is, the narrower peak we detect. The Q-factor of a peak at position λ_0 as defined as

$$Q = \frac{\lambda_0}{\text{FWHM}}, \qquad (3.1)$$

where FWHM is *full width at half maximum*. An equivalent statement is that a resonator can perform Q oscillations before its energy decreases down to $e^{-2\pi} \approx 0.2\%$ of its original value.

Here we compute Q-factor of the resonant peak when refractive index of investigated medium is set to $n_M = 1.3$.

In the following, we perform studies mostly on two-dimensional structures which lie in xy plane. We classify here two modes, TE^z and TM^z. Transverse electric contains E_x, E_y, H_z field components (p-polarization) and transverse magnetic H_x, H_y and E_z field components (s-polarization). Since Maxwell's equations are decoupled for these two polarizations, we can investigate them independently. Please note here that modes TE^z (TM^z) defined above in terms of the 2D plane normal correspond to the conventional TM (TE) modes respectively. These were defined in Sec. 2.3 with respect to the propagation direction along a common waveguide.

3.1   Hexagonal photonic crystal

The first structure is based on a hexagonal PhC waveguide where the middle row of holes is omitted to create the waveguide (so called W1-type PhC). The geometry is depicted in Fig. 3.2. The lattice constant is a and diameter of cylindrical holes is $d_1 = 0.65a$. The crystal consists of 17 times 18 holes, which can be filled
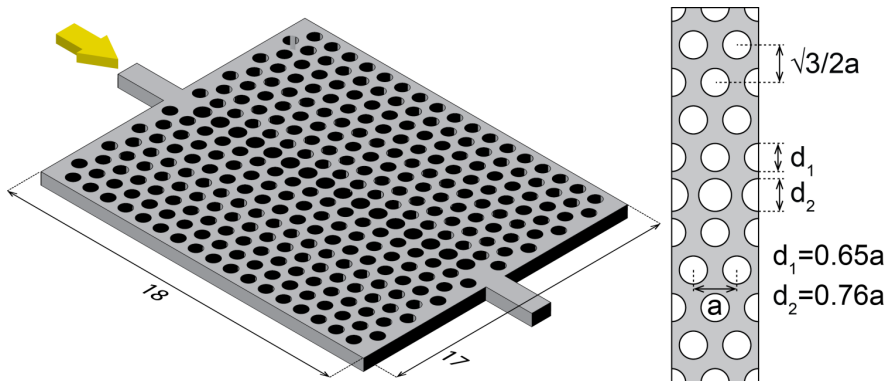

Figure 3.2: Geometry of hexagonal PhC. The lattice constant is a and hole diameter $d_1 = 0.65a$. Additional holes shifted of $a/2$ are added into the middle row to increase the sensitivity. Diameter of these holes is $d_2 = 0.76a$. The crystal consists of 17×18 holes. The polarization of incident light is TE^z and pulse is excited in the waveguide. Detector which detects transmitted light is placed inside the output waveguide.
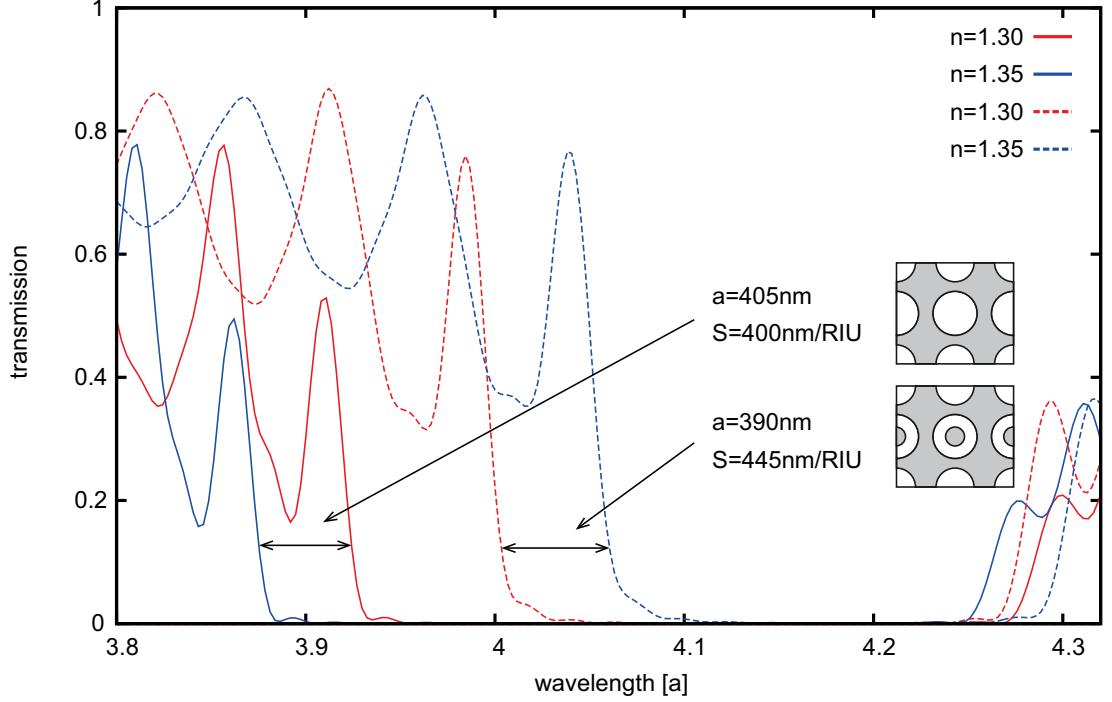
Figure 3.3: Transmission spectrum of hexagonal PhC with additional holes/rings added into the middle row to increase sensitivity. The sensitivity of original structure (empty middle row) was 120nm/RIU.

with a variable medium. The basic idea and parameters were taken from [35]. Good agreement of transmission spectra was achieved when same structure was simulated.

Nevertheless, to increase sensitivity we added additional holes shifted of $a/2$ with diameter $d_2 = 0.76a$ into the waveguide. The original sensitivity (when no holes were in the middle row) was 120nm/RIU and here we obtain $S = 400$nm/RIU.

If we suppose a bit more modified structure with rings (inner diameter $d_3 = 0.32a$) instead of holes in the middle row, we will get $S = 445$nm/RIU. But rings with inner diameter 125nm are definitely much more harder to fabricate than holes.

To obtain transmission spectrum as Fig. 3.3 shows, TE^z polarization is used. The resolution of Yee grid is high enough to obtain results with good quality. The lattice constant a consists of 37 points, i.e. $a = 37\Delta_x$. The diameter of holes is therefore represented by 24 grid points. Resolution in x and y direction is the same, $\Delta_x = \Delta_y$.

The last figure here, Fig. 3.4, demonstrates the spatial electric field intensity decomposition for broadband incident pulse. It can be seen, that some energy of pulse is dissipated in the crystal (it corresponds to wavelengths which are in the band gap) but lot of energy is transmitted through the crystal to the output waveguide. Figure also shows that the field is localized in holes filled with sensed medium, which enhances the sensitivity. When no holes were added in the middle row, the light did not interact with the medium intensively and the sensitivity on RI changes decreased.

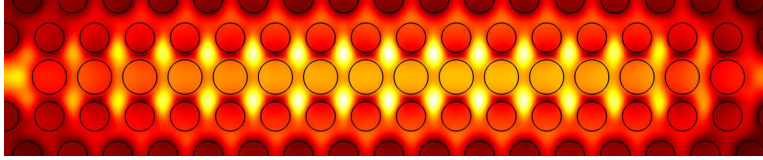If we want to examine a resonant peak instead of the band gap edge, we will

Figure 3.4: Spatial decomposition of electric field intensity. The field is localized in holes containing sensed medium and hence very high sensitivity on RI changes is observed.

create a resonant cavity inside the crystal. The simplest one can be created by removing one hole from the middle row. After that, the resonant peak should appear inside the band gap.

3.2 Chirped photonic crystal

To create an optical analogue of the well known and widely used electronic diode, the chirped photonic crystal was proposed [36]. Here, the violation of periodicity is used to create an asymmetrical light propagation. Due to unique crystal geometry, the intensity distribution on the output of the crystal is highly dependent on the direction of light propagation. Such structure can be used in all-optical computers as a diode. Furthermore, this chirped PhC also behaves as biosensor with a very good sensitivity.

The geometry of PhC with violated periodicity is depicted in Fig. 3.5. As figure shows, this is an inverted structure. Instead of holes we use dielectric rods here. The sensed medium is applied on the chip and flows between columns. The lattice constant a is preserved in direction perpendicular to light propagation but changes in the parallel direction. Distance between rows is linearly increasing from $0.5a$ to $3a$. The crystal consists of 11×10 columns. Since the structure is
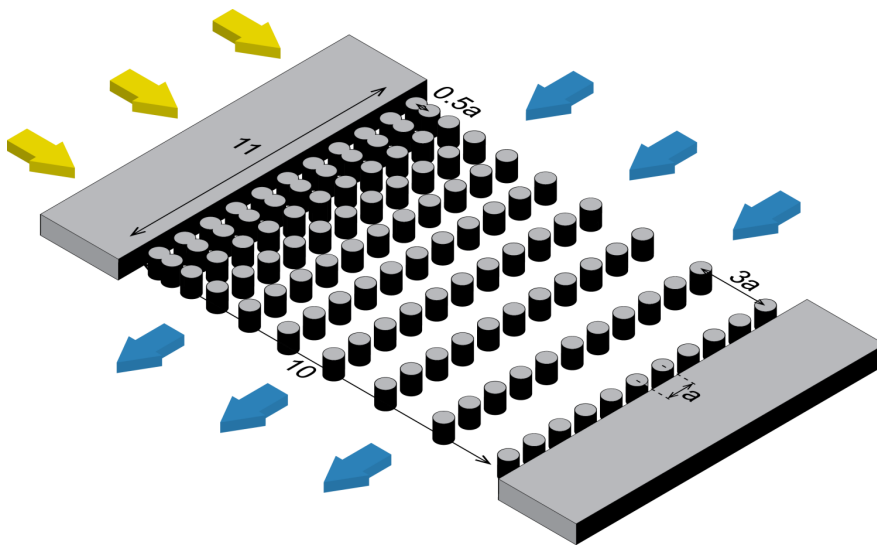

Figure 3.5: Geometry of the inverted chirped PhC. Instead of holes we use dielectric rods here and sensed medium flows between them. The distance between rows linearly increases from $0.5a$ to $3a$, radius of holes is constant $r = 0.3a$.
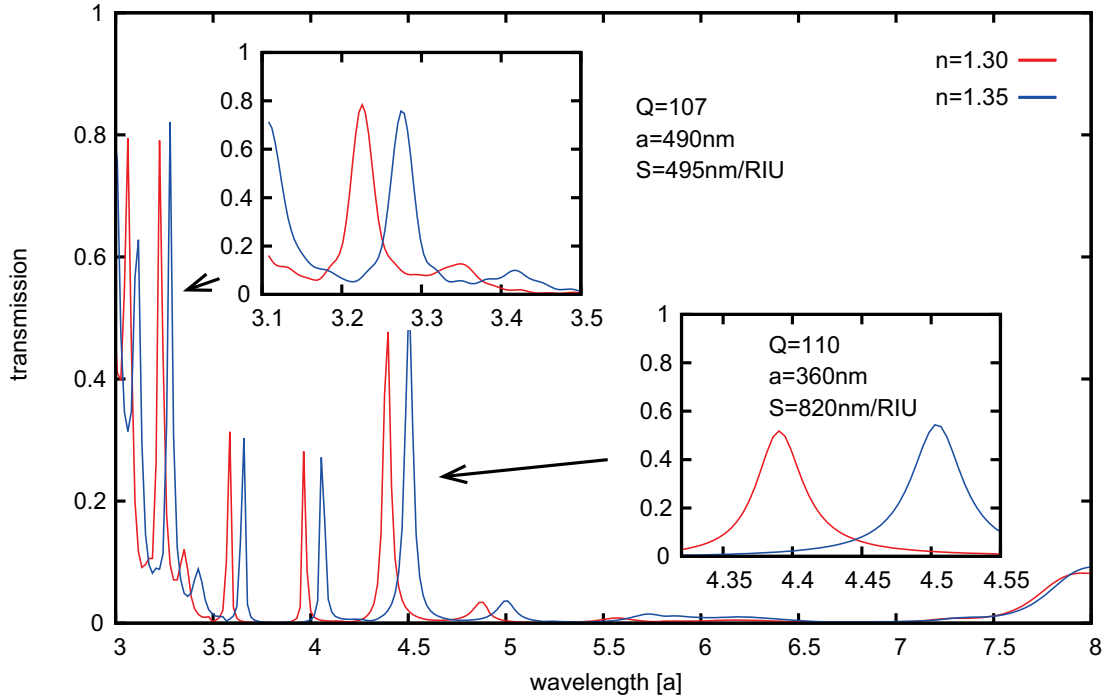
Figure 3.6: Transmission spectrum of chirped PhC as depicted in Fig. 3.5. As insets indicate, different peaks exhibit different sensitivity.

inverted, TM^z polarization is used to observe band gap[2]. Resolution of the grid is the same as in previous structure, $a = 37\Delta_x$.

Transmission spectrum of the inverted chirped PhC is displayed in Fig. 3.6. Due to violated periodicity, many resonant peaks appear in the band gap, which is more or less conserved. As figure and insets indicate, different peaks exhibit different sensitivity. Really high sensitivity ($S = 820$nm/RIU) is achieved in the case of one resonant peak. This high value again corresponds to very good light confinement as illustrated in Fig. 3.7.

The only fault here are very small Q-factors. Although peak position changes rapidly when compound with different refractive index is applied, we will not be able to recognize peak position precisely since the spectral line is too broad. The sensitivity is therefore not so high as we calculated here. The Q-factor could be probably improved by increasing number of periods.

Instead of improving this crystal we are going to analyse much simpler structure with comparable properties in the following chapter.
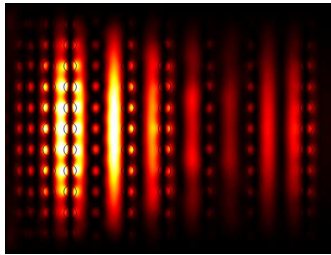

Figure 3.7: Electric field intensity in chirped PhC. Due to very good light confinement high sensitivity is achieved.

---

[2]TE^z-polarized light is concentrated in low-ε regions, whereas TM^z-polarized in high-ε regions. Due to low concentration factors of TE^z field components in dielectric rods we observe absence of the band gap. See [1] for further information.

4. Holey waveguide

Complex structures like PhCs described in the previous chapter can exhibit many phenomenal properties like bandgaps, narrow resonant peaks, asymmetrical light propagation or even nonlinear behaviour. These complicated structures are not usually easy to fabricate — and we are even not talking about three-dimensional PhCs which, more or less, still resist to our sophisticated fabrication methods.

In this chapter we propose quite simple and small photonic nanostructure, which is very easy to fabricate, very easy to implement into complex photonic chips, and as a biosensor exhibits comparable properties as advanced PhCs. This structure is based on a system presented in [37].

We take a simple dielectric waveguide and perforate it with periodic sequence of holes. The index-guided modes propagate along the waveguide without any losses, but the important photonic band gap appears in the transmission spectrum because of a defect in this periodic structure. This is done by separating two holes a bit more that others.

The very important thing is that we separate two holes a bit more. In this way we create a defect in the periodic sequence. As we will see, this defect will be responsible for resonant modes with the frequency inside the band gap.

4.1 One-dimensional case

Before we present our results of three-dimensional model it is useful to take look at a structure analogical to holey waveguide in one-dimension. Although we can obtain exact solution from 1D-FDTD we solve this simple structure via transfer matrix method.

The refractive index profile (Fig. 4.1) represents the cross-section of the holey waveguide along the propagation axis (x-axis in Fig. 4.18). Except of different medium in half-space of incidence and transmittance there is one very important difference to note. In the middle, there is a defect which violate the periodicity. This defect is responsible for a very important phenomenon called resonant modes.
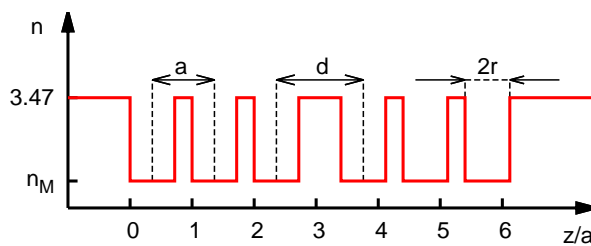

Figure 4.1: Refractive index profile of one-dimensional holey waveguide. Periodicity a, defect spacing d and "hole radius" r are defined in the figure. Refractive index of investigated medium is n_M.

4.1.1 Resonant modes

The periodicity of PhC induces its band structure. No modes are allowed to have their frequencies within the band gaps. But what happens when light with band gap frequency impacts the face of the periodic structure?

The situation is very similar to total reflection. The light is exponentially attenuated in the structure and is called an evanescent mode. Since all real wavevectors were used to construct dispersion relations, the wavevector K must be therefore complex (see (1.36)) and field is exponentially attenuated below the surface.

But if the evanescent mode is compatible with the structure and symmetry of a given crystal defect, it will propagate throughout the structure similarly to the electron tunnelling through potential barrier. The transmission of such mode can be very high, up to $T = 1$.

If we had an infinite PhC and we excited the resonant mode (eigenmode) right inside the defect, inside a resonant cavity, it could not propagate anywhere. We call it as localized mode. If the crystal was really infinite and no dispersion was present, the localized mode would stay inside the cavity forever — it would have an infinite lifetime and in transmission spectrum would be δ-function.

However, we are still not able to fabricate any infinite structures and dispersion more or less occurs everywhere due to absorption, scattering centres and inhomogeneities. Instead of δ-function we therefore detect broadened Lorentzian peaks at λ_0. The width of peaks is represented by Q-factor (3.1) as defined in Chap. 3.

4.1.2 Transmission spectra

Due to the crystal defect we expect detection of resonant peak, which is supposed to be inside the band gap. In the following, we are going to investigate behaviour of the 1D holey waveguide — simple PhC, where a is constant and d changes, $n_M = 1$. The final result is illustrated in Fig. 4.6. To understand it properly, we describe it step by step.

Figure 4.2: Transmission of 1D holey waveguide — PhC with defect. Defect spacing $d = 0.76a$, $r = 0.36a$.

We set $r = 0.36a$, hence $d > 0.72a$, angle of incidence is zero. Simple transmission for $d = 0.76a$ shows Fig. 4.2. Resonant peak is clearly visible in the middle of band gap. Let's move on and investigate dependence of peak position upon d. Several transmission spectra for different d are shown in Fig. 4.3. As figure shows, the peaks move to the right (lower energies) with increasing d. Until peak disappears on the right, new peak separates from the left, travel to the right and so on.

Full dependence of transmission spectra on defect spacing d is depicted in Fig. 4.4. The transmission spectra are plotted horizontally, one on the other. If d is small, only one resonant peak appears in the band gap. We may call it as the first peak. As d increases, the second peak separates from the left and so on. The bigger d is, the steeper lines signifying resonant peaks are. For very high d we would obtain many resonant peaks in the band gap. This example is demonstrated in Fig. 4.5, where $d = 2.5a$. If $d = a$ and thus no defect is present
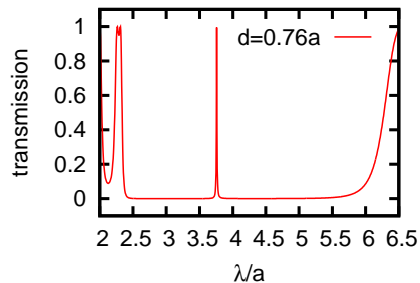
in the structure, no clear resonant peak is inside the band gap. Furthermore, we can see that the resonant peaks are the narrowest for $\lambda \approx 3.1a$ — somewhere around the first third of their travel throughout the band gap.
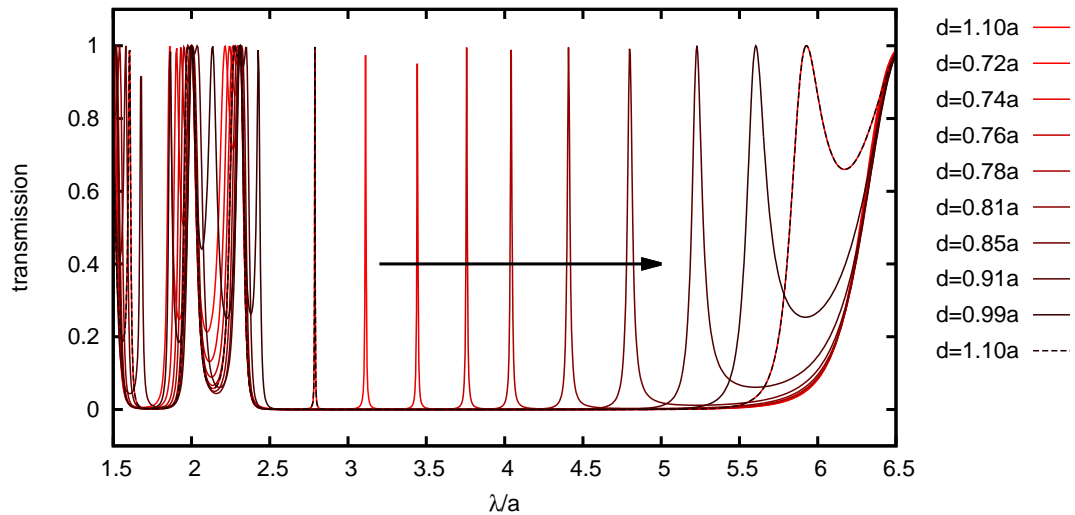

Figure 4.3: Several transmission spectra for different defect spacing d. When d increases, the resonant peak moves to the right. Until it disappears, new peak separates from the left and starts its travel throughout the band gap.
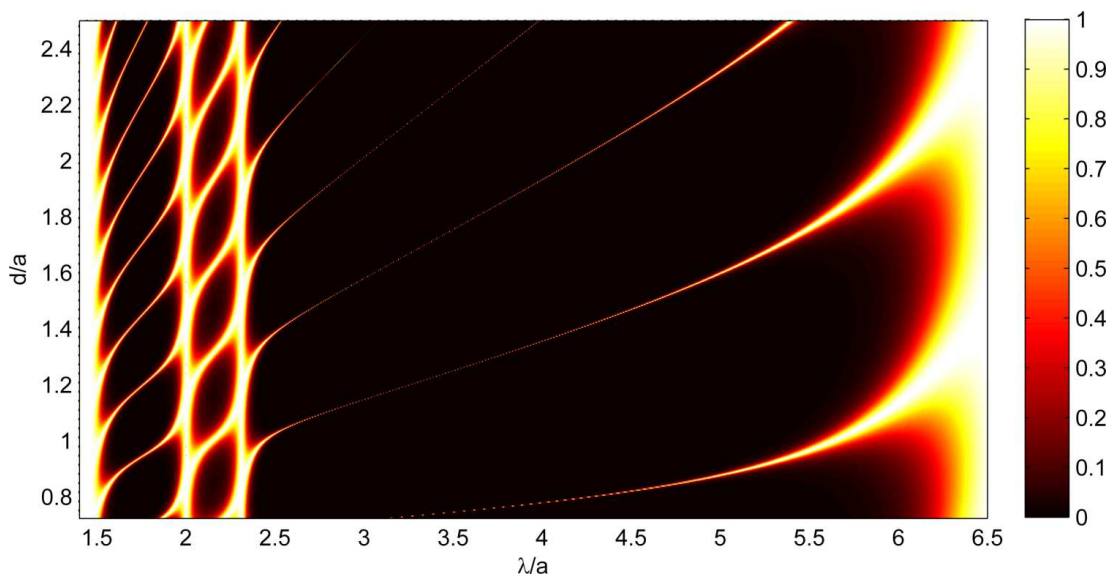

Figure 4.4: Set of transmission spectra in rows for various defect spacings d. Travels of resonant peaks throughout the band gap can be easily read from this figure. If d is small, just one resonant peak is inside the band gap. If d is large, many peaks appear in the band gap. Note, that any clear resonant peak appears in the band gap when $d = a$. In this situation no defect is present in the periodic structure.
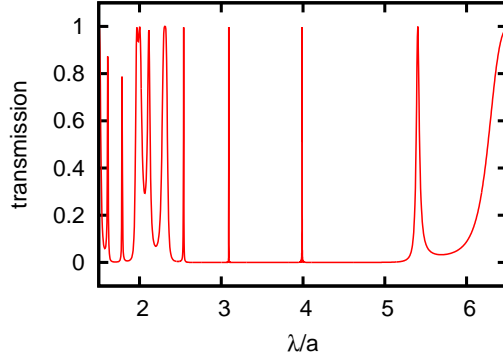
Figure 4.5: Transmission spectrum for $d = 2.5a$. Four resonant peaks are inside the band gap.

4.1.3 Resonant modes analysis

We finally come to the desired Fig. 4.6 which shows properties (sensitivity and Q-factor) of individual peaks upon parameter d. We can call it d-spectrum. In the interval $d \in (0.72, 1)a$ are properties of the first peak, in interval $d \in (1, 1.9)a$ are properties of the second peak and so on. Since there are four resonant peaks in the band gap for $d = 2.5$ (see Fig. 4.5), more blue and red lines representing sensitivity and quality are in Fig. 4.6 for $d = 2.5$. The results in Fig. 4.4 and Fig. 4.6 do not correspond precisely. This is because Figs. 4.3–4.5 are calculated for $n_M = 1$ and Fig. 4.6 for $n_M = 1.3$.

As the Fig. 4.6 with resonant peak properties shows, the best sensitivity is obtained when $d \approx 0.72a$, or when d is slightly bigger than a. Unfortunately, the Q-factors of the peaks are quite small at these defect spacings, hence the actual sensitivity to refractive index changes is small as well. We can say, that for $d \approx 1, 2$ we can get good sensitivity as well as high Q-factor.
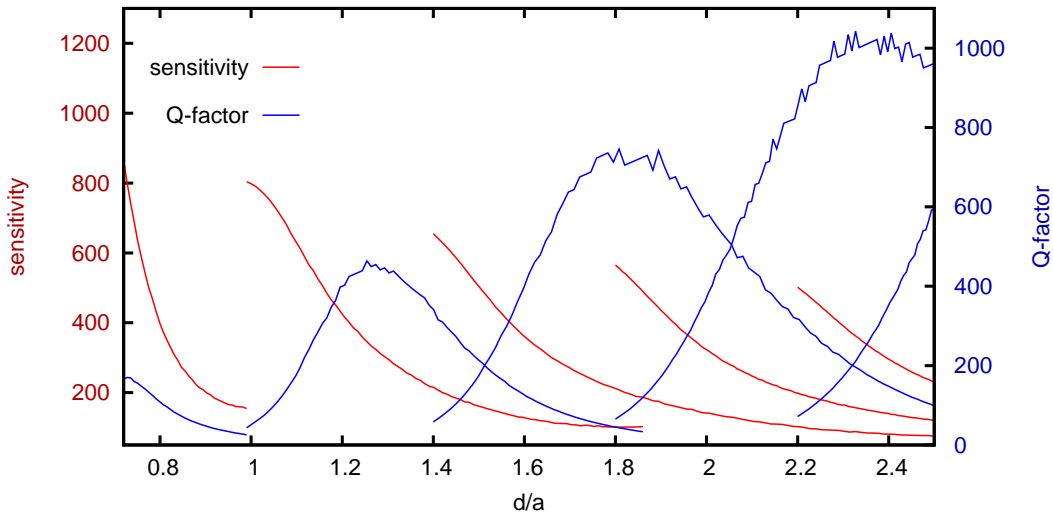

Figure 4.6: Properties of several resonant peaks. In interval $d \in (0.72, 1)a$ are properties of the first peak, in interval $d \in (1, 1.9)a$ are properties of the second peak and so on. Sensitivity is the highest when peak "appears" in the left side of band gap, but Q-factor is the worst at the same time. Blue lines, which represent Q-factors, are a bit noisy due to resolution of corresponding transmission spectrum from which the Q-factor was estimated.

One can see that some parts of Q-factor curves in d-spectrum are a bit noisy. It happens when the Q-factor is very high and not good enough resolution of transmission spectrum is used to estimate Q-factor.

4.1.4 Different number of holes in supercell

In previous paragraphs we assumed structure with two blocks (we call them supercells) separated by the defect spacing. Each supercell consisted of three "holes". We can mark this structure as 2×3. This nomenclature is used also in the next section, Sec. 4.2.

The next figure here, Fig. 4.7, demonstrates how is the Q-factor of resonant peak increasing when crystal consist of two supercells but different number of "holes". The dependence is clearly exponential.
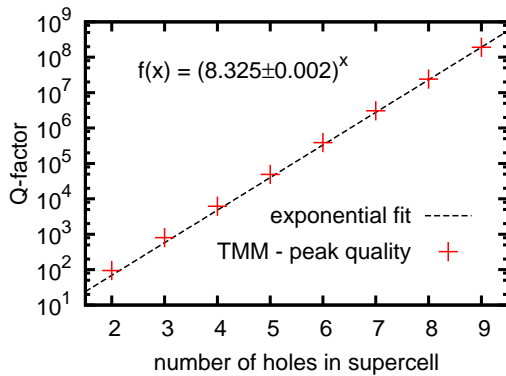

Figure 4.7: Exponential dependence of resonant peak quality on the number of "holes". When real structure is supposed, the dependence will not be exponential but saturates at Q_r (see equation (4.1)). Defect spacing is $d = 1.4a$ and "hole" radius $r = 0.36a$.

The high quality corresponds to long lifetime $Q^{(1)}$ of light which is trapped inside the defect. In real structures we unfortunately do not obtain so nice exponential dependence. The lifetime Q includes two different decay channels. The light decays from the cavity into the crystal with lifetime Q_c. Except of that, it also radiates outside the crystal sample (i.e., to the surrounding medium, to the substrate when 2D photonic crystal is assumed, outside the waveguide, etc.) with lifetime Q_r. Therefore we get [16]

$$\frac{1}{Q} = \frac{1}{Q_c} + \frac{1}{Q_r}. \tag{4.1}$$

When $Q_c \to +\infty$, the Q saturates at Q_r. Due to inhomogeneities and finite size of samples we cannot actually achieve infinite lifetime, we cannot stop the light in the cavity and we cannot detect δ-function in transmission spectrum.

The last thing we investigate here is the dependence of the transmission spectrum on the refractive index n_M. We described sensitivity of several peaks in previous paragraphs and visualized it in Fig. 4.6. Here we investigate a behaviour of only one peak, the second one, for $d = 1.4a$. The result is depicted in Fig. 4.8. Transmission spectra are plotted horizontally, one on the other, similarly as in

---

[1]From Fourier trasform it is clear that with higher Q-factor the lifetime of resonant mode is longer. Therefore, let us mark the Q-factor and corresponding lifetime with the same letter Q.

Fig. 4.4. If $n_M = 1$, the peak position is about $4.1a$. As the refractive index in "holes" changes, the peak moves to the right. As figure shows, the Q-factor of the peak decreases for higher n_M. If $n_M = 3.47$, the transmission must be exactly one because the crystal becomes a homogeneous medium.

To conclude our efforts so far, we will bring our focus to the region $d \in (1, 1.6)a$ when simulating higher dimensional structures, since we expect only one resonant peak in band gap and high sensitivity. The Q-factor might be probably increased by adding additional holes.
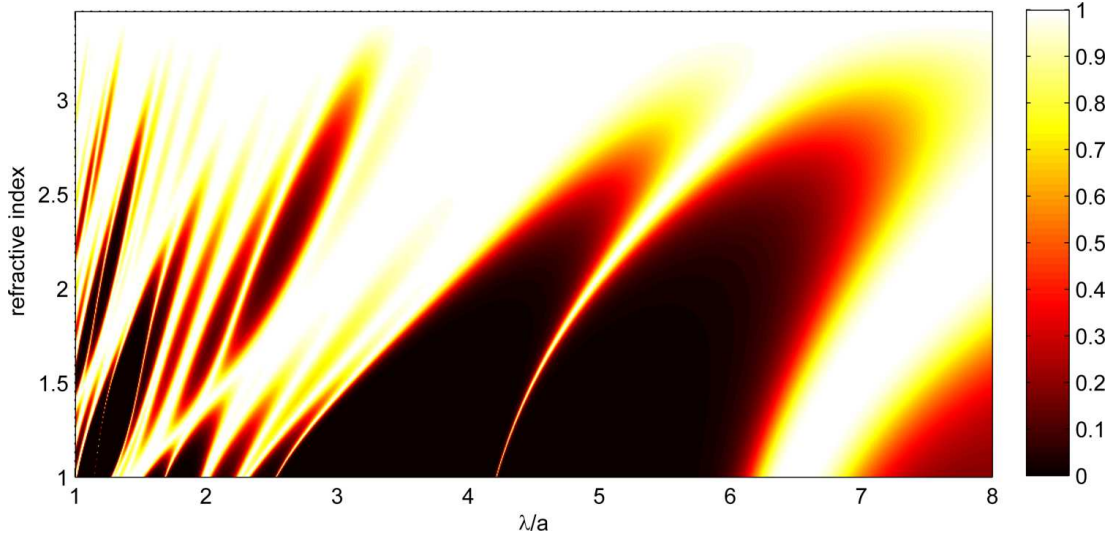

Figure 4.8: Transmission spectrum as a function of the refractive index n_M. Defect spacing is $d = 1.4$. The behaviour of the second peak is depicted here. In accordance with Fig. 4.4, the peak position is about $4.1a$ for $n_M = 1$. The transmission is one for all wavelengths when $n_M = 3.47$, because crystal transforms to homogeneous medium.

4.2 Two-dimensional case

We have done quite a lot of studies on one-dimensional system and now is good time to do a step forward to the second dimension. Before we will investigate complex three-dimensional structure, we compute parameters of 2D model with the hope of determining main physical properties.

The geometry of our model is depicted in Fig. 4.9. Since the 2D case is assumed, we do not model any SiO_2 buffer and we set infinite height of waveguide, $h \to \infty$. In contrast to 1D system, where normal incidence was modelled, we have to choose particular polarization of the incident light. To observe band gap and resonant peaks we choose TE^z polarization here (E_x, E_y, H_z).

The transmission spectrum of this 2D holey waveguide is very similar to transmission spectrum obtained from TMM, Fig. 4.2. These spectra together with 3D case are compared in detail in the next section, Sec. 4.3. We focus to enhancement of parameters like sensitivity and Q-factor via geometry modifications now. The goal is obvious — find d, r and number of holes which maximize both S and

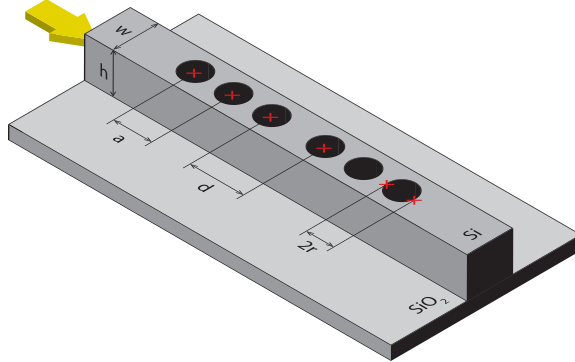Q. The resolution is set as $a = 50\Delta_x$.

Figure 4.9: This picture illustrates 3D model, where the silicon waveguide of height h is placed on SiO_2 buffer. Here we suppose only 2D waveguide in vacuum or sensed medium. Definition of period a, defect spacing $d = 1.4a$ and hole radius $r = 0.36a$ remain unchanged and width is defined as $w = 1.2a$.

4.2.1 Even and odd eigenmodes

Before we start with structure modifications, we take a look at eigenmodes propagating through the waveguide. The theory of eigenmodes in planar symmetric waveguide was briefly mentioned in Sec. 2.3 and hence we know how to excite particular mode into the waveguide in FDTD. We used broadband pulse (sinus modulated with Gaussian profile, $\lambda = 4a$) to obtain wide transmission spectrum. Since the parameters (polarization and ratio wavelength/thickness) of waveguide and incident light are defined as before, we know that only two modes (even and odd) can propagate through the waveguide. See Fig. 2.6, where the field distribution of these modes is depicted.

The comparison of optical response of the even and odd mode is illustrated in Fig. 4.10. Figure 4.10a depicts magnetic light intensities integrated over very long time (till stored energy in the defect becomes negligible, $t = 10^5\Delta_t$), whereas Fig. 4.10b compares transmission spectra, $n_M = 1.3$.
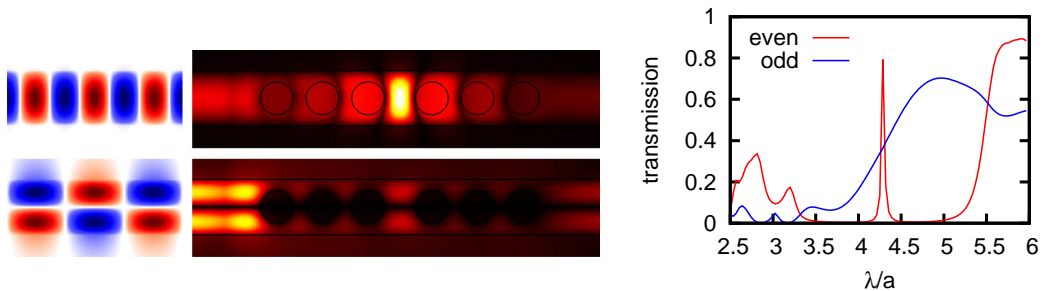
(a) Magnetic light intensity integrated over very long time. Top: even mode, bottom: odd mode.

(b) Transmission spectra of even and odd mode propagating through the holey waveguide.

Figure 4.10: Even mode has much of its power concentrated inside the holes but field of odd mode is distributed in the surrounding dielectric. This fact explains the big difference in the transmission spectra. The resonant peak at $\lambda \approx 4.3a$ in (b) corresponds to the trapped light inside the defect which might be clearly visible in (a), top.

The spectrum obtained for even mode exhibit very nice and broad band gap with a resonant peak in the middle. No resonance nor the band gap is visible when odd mode propagates through the waveguide. Therefore, all further simulations we excite the first even mode to the grid.

4.2.2 Q-factor determination

Since we use time domain simulation, determination of high-quality peaks might be not as easy as with TMM. If the resonant peak is very narrow, the light is trapped in the cavity for a very long time and radiation to surrounding is very slow. To determine Q-factor of such resonant peak exactly, we would have to integrate Maxwell's equation over very long time. Therefore, we use here slightly different and more accurate way to compute Q-factor [37]:

$$Q = \frac{\omega E}{P} = -\frac{\omega E}{\mathrm{d}E/\mathrm{d}t} \quad \Rightarrow \quad E \approx \exp\left(-\frac{\omega}{Q}(t - t_\mathrm{D})\right), \quad (4.2)$$

where E is stored energy, ω is the resonant frequency, $P = -\mathrm{d}E/\mathrm{d}t$ is the dissipated power and t_D is the time when exponential decay of stored energy starts. In FDTD it means, we compute the stored energy in every time step and in postprocess we fit the data with the exponential function. The result is shown in Fig. 4.11. The first part corresponds to the light pulse excitation, reflection and dispersion. When the light is scattered and only resonant mode remains in the defect cavity, slow exponential decay of stored energy is started. The last part of decay corresponds to non-physical processes — the numerical errors caused by
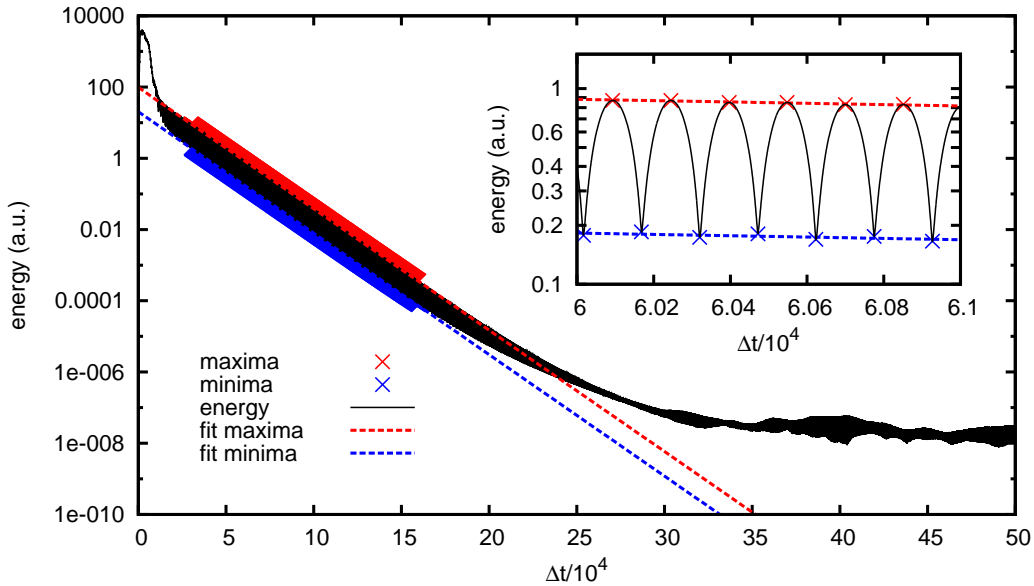

Figure 4.11: Exponential decay of energy trapped in the defect. After the excitation, which corresponds to the first part, the resonant mode starts its slow exponential decay. Last part corresponds to numerical errors. Computed Q-factors are $Q_\mathrm{max} = (131.4 \pm 0.1)$ and $Q_\mathrm{min} = (131.3 \pm 0.2)$.
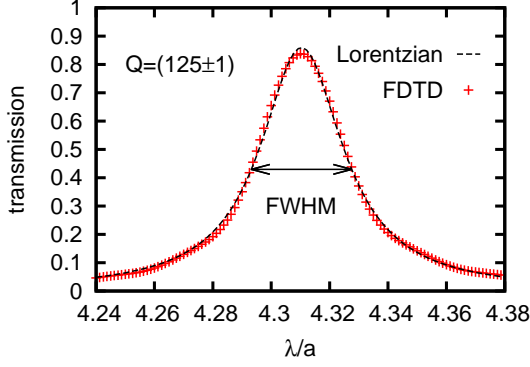
Figure 4.12: Transmission spectrum of holey waveguide. Resonant peak in the middle of band gap has Lorentzian shape. Using the fit we can calculate Q-factor as $Q_{RP} = (125 \pm 1)$.

non-zero reflectance of PML boundaries, round-of error and others. With respect to the logarithmic scale, these errors might be confidently neglected.

Part of transmission spectrum containing focused to resonant peak is in the Fig. 4.12. According to the theory [1], the profile of the peak is Lorentzian. By fitting computed data we can estimate Q-factor as $Q_{RP} = (125 \pm 1)$. The Q-factor obtained from energy decay is $Q_{ED} = (131.4 \pm 0.1)$. These two values are very close. Since Q_{RP} is computed from transmission spectrum, which is obtained via Fourier transform which requires integration over time from zero to infinity, we may expect $Q_{RP} \leq Q_{ED}$, which is true. If we do the same procedure for more narrow peaks, we will get bigger and bigger difference.

The observation the process of energy decay as shown in Fig. 4.11 is useful even for other purposes than estimation of Q-factor. If we zoom to short time period, we will see oscillations of the energy stored in the defect (as the inset in Fig. 4.11 shows). The period of oscillations is $152\Delta_t$. Using the relation $\lambda = cT$ we get the wavelength of oscillating mode $\lambda = 4.31a$, which exactly corresponds to the position of resonant peak in transmission spectrum, Fig. 4.10b. Why is it useful? If there are more resonant modes, we will apply Fourier transform to oscillations in energy decay and calculate wavelengths of oscillating modes even without calculating transmission spectrum! This might be very useful when high-Q mode with unknown resonant frequency is present. The determination of the position of such high-Q peak using only transmission spectrum might be very difficult and tedious.

We use the definition of Q-factor (4.2) to determine exponential dependence as investigated before (Fig. 4.7). Parameters like d or r remain unchanged but
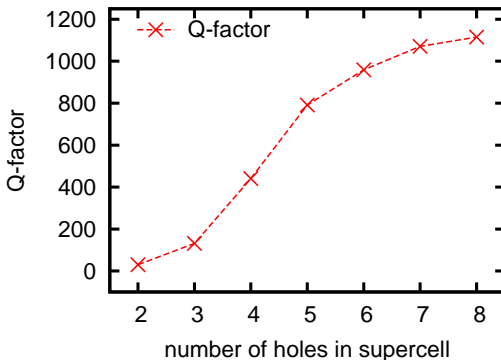

Figure 4.13: Dependence of Q-factor upon the number of holes in one of two supercells. Exponential growth is visible only for small number of holes, then Q-factor saturates at value about 1100.

number of holes in each of two supercells is changed. The clear exponential function is not present here. Instead, as can be seen in Fig. 4.13, the formula (4.1) describes this behaviour better. The Q-factor saturates around value $Q_r \approx 1150$ due to the leakage of radiation to surrounding medium. Therefore, Q-factor cannot be increased by adding more and more holes keeping only two supercells.

4.2.3 Geometry modifications

In the following, we consider $d = 1.1a$, $r = 0.36a$ and three supercells each of three holes, 3×3 — unless otherwise stated.

First of all, we estimate what happens with S and Q when the spacing between holes a and radius r are changed[2]. The changes are illustrated in Figs. 4.14. As Fig. 4.14a shows, even higher sensitivity than 600nm/RIU might be obtained. Unfortunately, the Q-factor as well as clearance of the resonant peak rather decreases with growing r. Considering these two figures (Figs. 4.14a, 4.14b) we decided to keep $a = a_0$ and $r = 0.36a_0$.
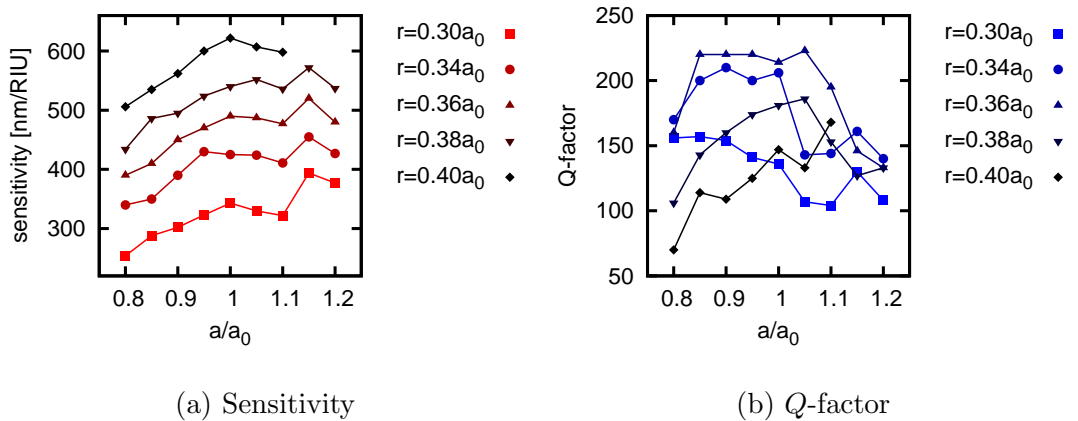

(a) Sensitivity

(b) Q-factor

Figure 4.14: Dependences of the sensitivity and Q-factor on period a and hole radius r are changed. Even higher sensitivity than 600nm/RIU can be achieved unless we are not too interested in high Q-factor. Note that each point in (a) was obtained by running two simulations (two different RIs).

The next step is to observe what happens if the spacing between supercells, i.e. defect spacing d, varies. Comparison of S, Q and transmission spectra is illustrated in Fig. 4.15. Here it is worth to compare the properties of the second peak in Fig. 4.6 with properties shown in Fig. 4.15a. Although the geometries vary quite a lot and totally different approaches were used to obtain this behaviour, the dependences of S and Q upon d are very similar. Here we decided to set defect spacing as $d = 1.1a$.

The very useful feature for biosensor is linear dependence of resonant peak position upon the refractive index of sensed medium n_M (that also means constant sensitivity). Many peaks for varying RI are shown in Fig. 4.16b. Obviously, the peak is being wider and wider when RI increases since there is lower contrast

---

[2]In this part we denote a_0 as the main, unchanged parameter (i.e., $d = 1.1a_0$, $w = 1.2a_0$, $r = 0.36a_0$) and a as the spacing between holes in supercell.

(a) Sensitivity and Q-factor.

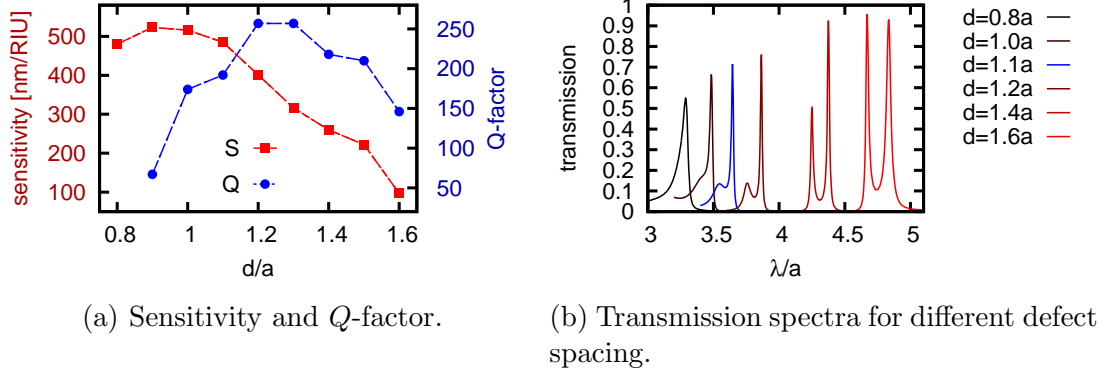(b) Transmission spectra for different defect spacing.

Figure 4.15: Profiles of sensitivity and Q-factor in (a) are nearly the same as in one-dimensional case (see Fig. 4.6). The resonant peak profiles are compared in (b). Two resonant peaks appear for higher d. Considering these both figures we chose $d = 1.1a$ for further simulations.

between refractive index of silicon and sensed medium. Almost perfect linear function is displayed in Fig. 4.16a.

The last parameters we change here, in two dimensional holey waveguide, are the number of supercells and number of holes in each of them. The results are shown in Figs. 4.17. It is obvious that Q-factor grows when more holes are perforated into the waveguide. The other notable thing is that sensitivity is not growing with more holes, but saturates about 500nm/RIU. Therefore, adding more holes is useful only if higher Q-factor has to be obtained.

Nevertheless, with increasing number of supercells the number of resonant peaks in the band gap increases as well. This fact is also demonstrated in Tab. 4.1, where columns indicate number of supercells and rows number of holes in each supercell. For simplest determination of the peak position is the best only one resonant peak.

(a) Resonant peaks for different n_M.
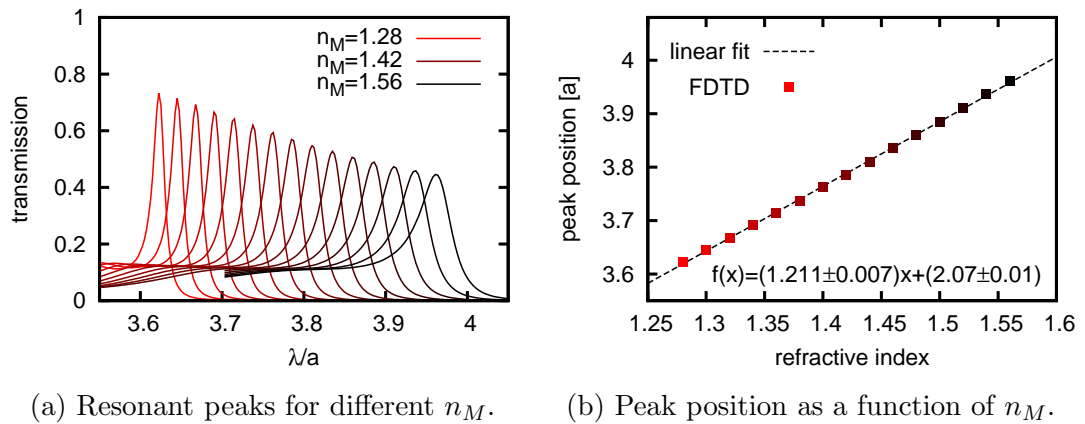
(b) Peak position as a function of n_M.

Figure 4.16: These figures demonstrate linearity of resonant peak position upon the refractive index of sensed medium n_M. This feature is very useful for biosensing.
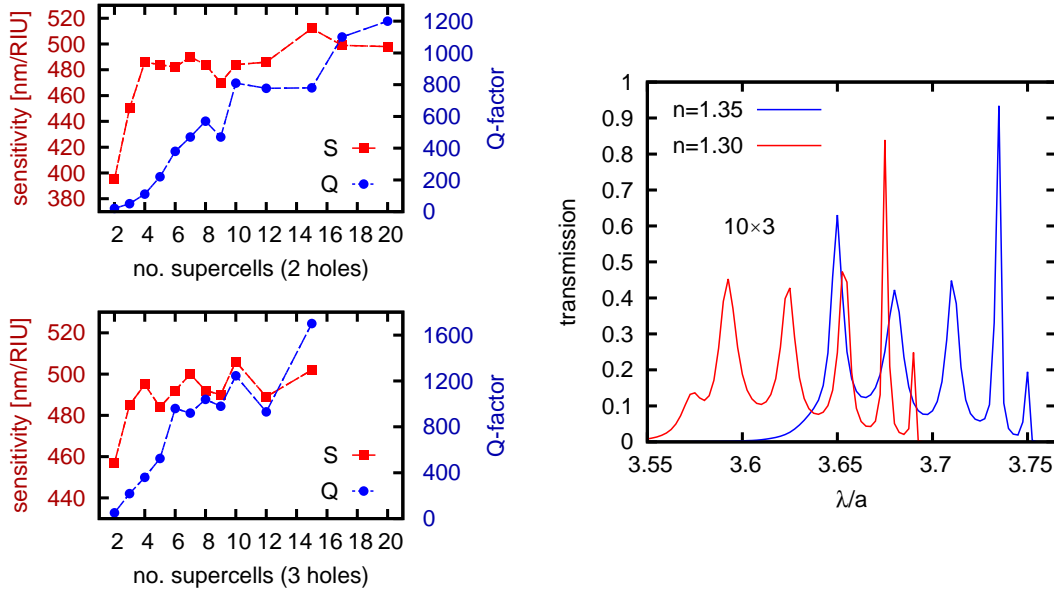
Figure 4.17: Dependence of S and Q upon the number of holes. As can be seen, Q-factor increases with number of holes, whereas sensitivity saturates at ≈ 500nm/RIU. Figure on the right compares transmission spectra of waveguide with ten supercells with three holes for two different refractive indices. Five resonant peaks are present. The Q-factor was computed from the narrowest peak using definition (3.1).

H\S	2	3	4	5	6	7	8	9	10	12	15	17	20
2	1	1	1	1	2	2	2.5	3	3	4	5	6	8
3	1	1	1.5	2	3	3	4	4	5	6	8	9	11
4	1	1	2	3	4	4	4	5	5	6			
5	1												

Table 4.1: Number of resonant peaks in the band gap for different number of supercells and holes. Columns indicate number of supercells and rows number of holes in each supercell. For instance, eleven peaks will be in the band gap, if twenty supercells of 3 holes (together $20 \times 3 = 60$ holes) are in the waveguide. The non-integer numbers indicate, there is one additional peak with certain ratio. The empty cell means that no simulation was done for these parameters or transmittance was too small.

4.3 Three-dimensional case

In this section we compare results of all n-dimensional cases (n=1,2,3) and investigate behaviour of 3D silicon holey waveguide situated in the air and on a SiO_2 buffer. At the end we simulate how fabrication deviations can affect physical properties of the modelled structure.

Analogically as before, we set width $w = 1.2a$, height $h = w$, defect spacing $d = 1.4a$, hole radius $r = 0.36a$, refractive index of silicon waveguide $n_{Si} = 3.47$ and SiO_2 buffer $n_{SiO_2} = 1.44$. The even TE^z mode is excited in the yz-plane for $x = 8\Delta_x$ and the transmitted light is detected in the middle point in the end of the waveguide[3].
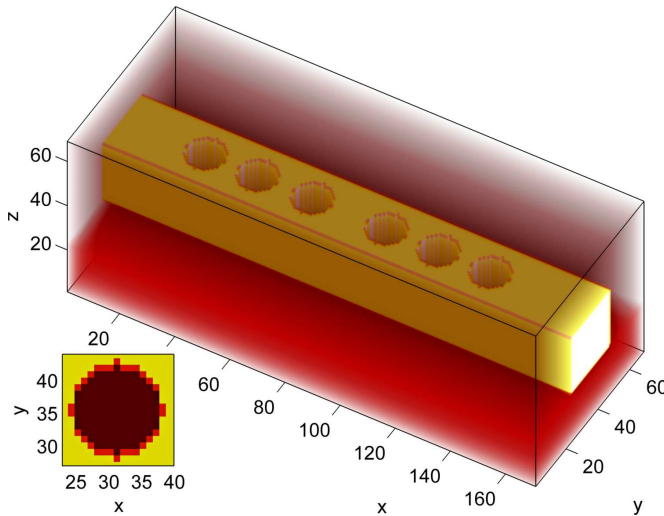

Figure 4.18: The figure shows relative permittivity of silicon holey waveguide situated on the SiO_2 buffer. The resolution of Yee grid is set to $a = 19\Delta_x$ and holes are therefore represented by 14 cells. Note that edges have different colour due to sub-cell averaging.

4.3.1 Comparison of 1D, 2D and 3D results

Since the calculation of the band gap and peak position were actually done, we may start with the transmission spectrum. The four spectra are compared in Fig. 4.19. The first one is obtained from the TMM where normal incidence on the layered structure (Fig. 4.1) is assumed. The second spectrum is assigned to 2D-FDTD and the third and fourth to 3D-FDTD where the waveguide is situated in the air (or sensed medium) and on the SiO_2 buffer, respectively.

The spectra are more or less very similar. As might be expected, the band gap is the narrowest for 3D case and the widest for 1D case since the periodicity is the most ideal in 1D structure. Due to the same reason, even Q-factor of resonant peak decreases with complexity of the geometry. Since the position of the peak is highly sensitive on defect spacing, we attribute varying position of the resonant peak mainly to the not ideal resolution of the grid in FDTD.

Figure 4.20 compares transmission spectra of 3D holey waveguide on SiO_2 buffer for several different heights. Position of resonant peak slightly varies, but main physical properties of the structure remain more or less unchanged. Peaks are not very high because simulations were not computed for sufficiently long time and lots of energy remained trapped in the defect.

---

[3]The light was also detected in the whole waveguide cross-section and very similar results
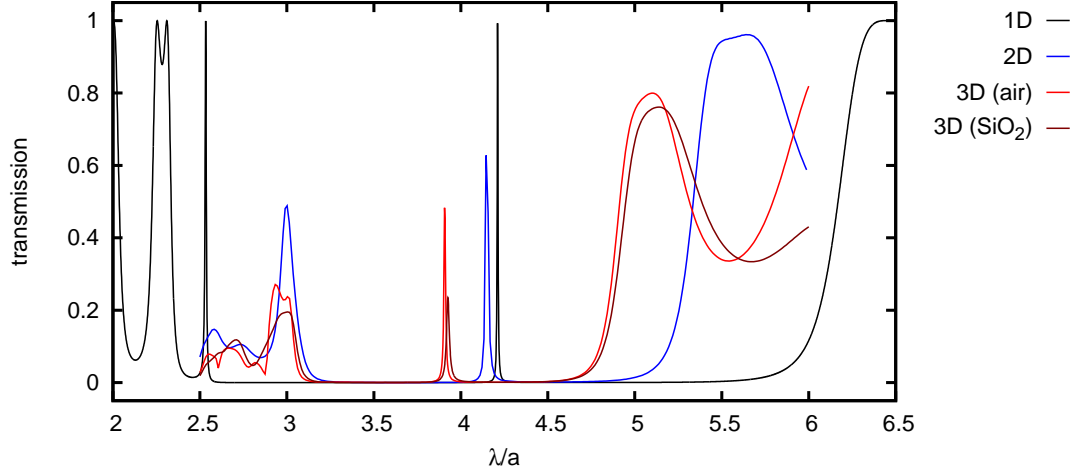
Figure 4.19: Comparison of transmission spectra of one-, two- and three-dimensional holey waveguide. Different positions of resonant peak are partially attributed to small resolution of Yee cell. The waveguide is surrounded by air ($n_M = 1$).
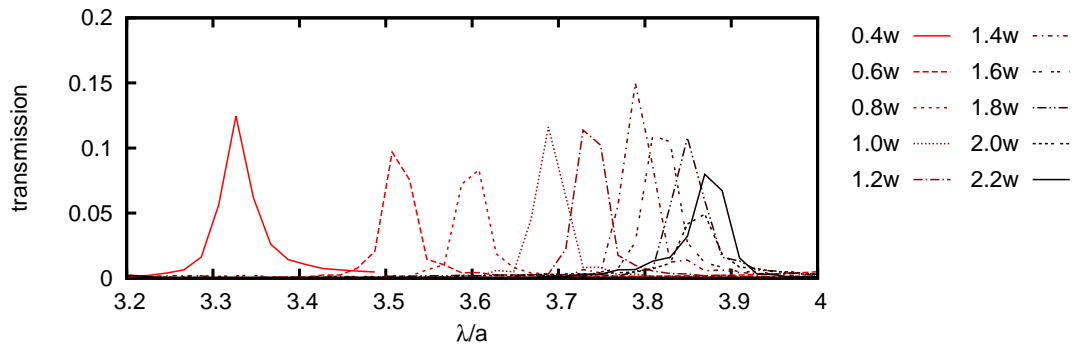

Figure 4.20: Comparison of transmission spectra of 3D holey waveguide on SiO_2 buffer for different heights h when $n_M = 1$. The peak position varies, but other properties like sensitivity and Q-factor remain unchanged. In our simulations we set $h = w$.

With respect to results from lower-dimensional simulations we try to decrease defect spacing to achieve higher sensitivity. Unfortunately, the Q-factor of resonant peak decreases very fast until it completely disappears. The dependence of S and Q is illustrated in Fig. 4.21, where is the d-spectrum compared with TMM and 2D-FDTD. Very similar behaviour of the physical properties is observed.

Now we compare Q-factor dependence on number of holes in one supercell for all n-dimensional cases ($n = 1, 2, 3$). The comparison is showed in Fig. 4.22. Very fast exponential growth can be seen in one-dimensional case. The more complex structure is considered, the smaller Q-factor of resonant peak is observed.

---

were obtained. To decrease large computational time we detected light just in one point.
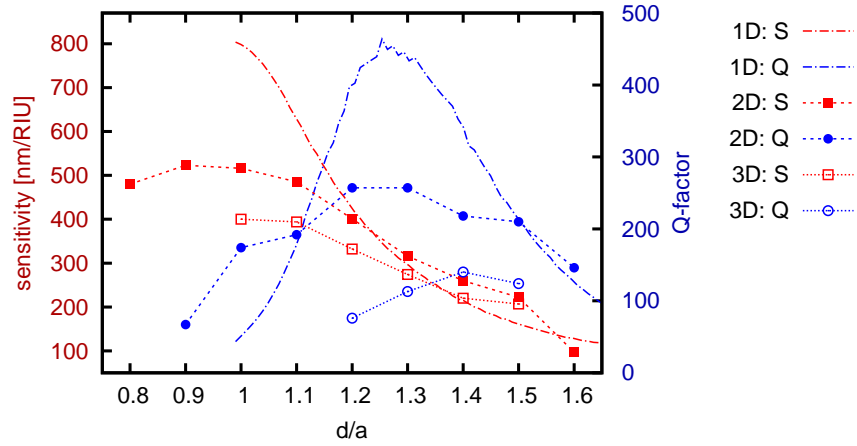
Figure 4.21: Comparison of d-spectra of 1D, 2D and 3D holey waveguide. In 3D (with SiO_2 buffer), there is no resonant peak in spectrum for $d < 1.2a$ and sensitivity is measured using cut-off wavelength.
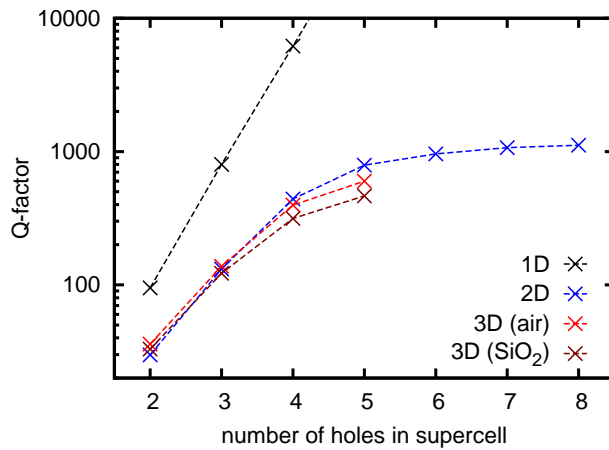
Figure 4.22: Comparison of Q-factor dependence upon number of holes in one supercell for all n-dimensional cases. The refractive index of investigated medium is supposed to be $n = 1.3$. These results are also partially showed in Fig. 4.7 and Fig. 4.13.

4.3.2   Fabrication deviation

Although nanotechnology industry is growing in tremendous rate and uses high-ly sophisticated methods like lithography, 3D printing, ion or electron beams and many others, certain deviations from the desired accurate structure are still present. Therefore, we examine properties of our model with some particular deviations.

Conical and cylindrical holes

First of all, we compute sensitivity and Q-factor when conical instead of cylindri-cal holes are perforated into the waveguide. The conical shape of holes is often investigated since it is common shape of fabricated holes and it might leads to decrease or failure of desired physical properties [38].

Here we denote $r_0 = 0.36a$ as the top radius and r_2 as the bottom radius of the cone. The sensitivity and Q-factor are in the Fig. 4.23a, the transmission spectra in the Fig. 4.23b. As figures show, the smaller r_2 is (the more conical holes are), the smaller values of S and Q we obtain and the band gap is more and more violated. Therefore, the fabrication process should be definitely focused on ideal cylindrical hole perforation.
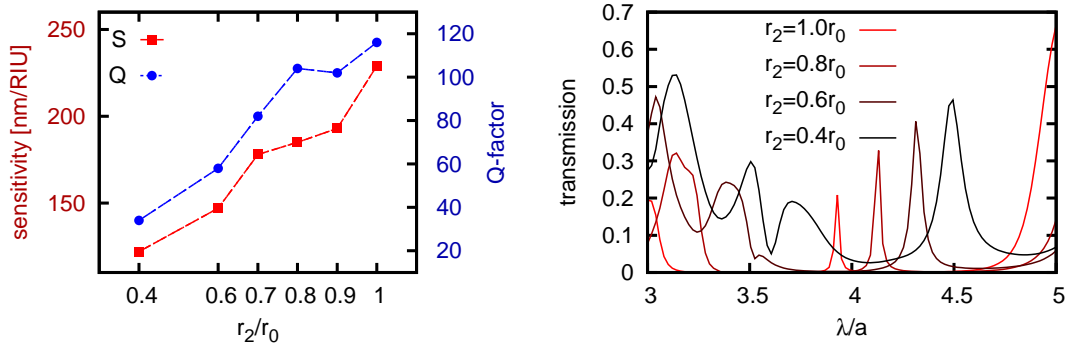
(a) Sensitivity and Q-factor.   (b) Transmission spectra.

Figure 4.23: The (a) shows sensitivity and Q-factor when conical holes are present. Here, r_0 is the top radius and r_2 is radius at the bottom of the cone. For $r_2 < r_0$ the higher waveguide should be probably modelled to achieve band gap and clear resonant peak.

Deviation in the radius and position

It the next step, we consider small deviation in the radius and the position of the hole. To produce more realistic results, we assumed here also partially conical holes: $r_2 = 0.8r_0$. We denote here hole with letter H and assign it parameters r_0 for radius and x_0 for exact position. A deviation from its exact and desired shape might be defined as

$$H(r, x) = H[r_0(1 + \xi), x_0(1 + \xi)], \tag{4.3}$$

where ξ is a random number lying in interval $(-\xi_m, \xi_m)$, which is limited by maximal deviation ξ_m. The value $\xi_m \cdot 100\%$ is therefore maximal percentual deviation from the right shape. The results are presented in the Tab. 4.2. Ten simulations were done for $\xi_m = 5\%$ and $\xi_m = 10\%$ to obtain some reasonable statistical results. The table also compares parameters S and Q when no deviation is present and even when holes are perfectly cylindrical.

To summarize the results the Tab. 4.2 shows, we can say that the deviation error up to 5% does not affect sensitivity neither Q-factor too much and the emphasis should be put especially to the cylindrical shape of holes.

Taking in account that resonant peak is at position $\lambda \approx 4.3a$, diameter of holes is $0.72a$, maximum deviation is $\xi_m = 5\%$, we want to observe peak at 1550nm, we get that sizes of the holes should not differ more than 13nm.

		1	2	3	4	5	6	7	8	9	10	mean	$\xi_m = 0$ $r_2 = 0.8 r_0$	$\xi_m = 0$ $r_2 = r_0$
$\xi_m = 5\%$	S	181	210	175	177	205	196	205	145	150	152	(180 ± 24)	$S=185$	$S=221$
	Q	95	103	96	100	112	87	90	87	84	92	(95 ± 9)		
$\xi_m = 10\%$	S	150	192	210	183	169	228	134	270	180	111	(183 ± 46)	$Q=104$	$Q=121$
	Q	67	61	72	85	54	72	66	66	61	83	(69 ± 10)		

Table 4.2: Comparison of sensitivity and Q-factor when deviation of holes from accurate position and radius is present with the case when conical and perfectly cylindrical holes at appropriate position are assumed.

Conclusion

In attempt to simulate light scattering and propagation through photonic nanostructures the complex three dimensional FDTD code has been written. We have started with discretization of Maxwell's equations to make them readable for computers, and after some more manipulations we have obtained so-called update equations which form the core of Yee's algorithm.

Numerous extensions have been added to our code to obtain frequency-dependent transmission spectra, to simulate free space, or to observe plane wave propagation. The code has been tested using simple model simulations like grid scattering or diffraction on circular slit, where reasonable agreement with different numerical or even analytical approaches has been achieved. We have also shown that using non-constant spatial step (the simplest case of nonorthogonal grid) the magic time-step might be achieved in one-dimension even if dielectric materials are considered. That lead us to exact numerical solution up to round-off errors.

Brief introduction to the transfer matrix method has been provided to compare results with FDTD and to analyse photonic structures more precisely. TMM has been demonstrated upon the Bragg mirror.

Using our debugged FDTD code we have computed transmission spectra of W1-type hexagonal PhC and proposed slightly modified geometry for enhanced sensitivity of biosensing devices. The sensitivity has been increased from 120nm/RIU to 400nm/RIU.

We have also found out that chirped PhC, originally proposed as optical diode, might be used for biosensing, since it exhibits very strong sensitivity on refractive index changes ($S = 820$nm/RIU).

Finally, we have shown that even much more simple structure than PhCs, known as holey waveguide, may exhibit important features like band gap and resonant modes. We have assumed silicon waveguide situated on the SiO_2 buffer. Several blocks of holes (called supercells) have been perforated into the waveguide, separated by defect spacing. The internal periodicity of supercells caused the presence of photonic band gap, whereas violation of periodicity between supercells induced resonant modes which might be visible in transmission spectrum as narrow peaks.

Simplified 1D model has provided us very detailed behaviour of resonant modes upon the size of defect spacing, refractive index of sensed medium and also upon the number of layers. Keeping in mind these results, we have modified geometry parameters of 2D model to achieve high sensitivity and Q-factor. The highest sensitivity we achieved has been $S \approx 500$nm/RIU and Q-factor $Q \approx 1000$. The most realistic model of holey waveguide has been simulated using 3D-FDTD. The best properties for biosensing should be obtained when waveguide is not lying upon any buffer but is situated in the air like a bridge. When fabricated, sensitivity about 300nm/RIU should be measured and Q-factor about 500 or maybe even more should be achieved by increasing number of holes in supercells.

In conclusion, the study of simplified one-dimensional model is very useful to understand the behaviour of main physical properties of the real structure.

More precise and accurate simulation using three-dimensional model has shown, that relying only on 1D or even 2D model might lead us to overestimation of crucial physical properties. According to our simulations, the holey waveguide may definitely compete with more complex PhCs in the biosensing field. The fabrication should be focused on perforating cylindrical and not conical holes, and the smallest resolution about 13nm should be required.

Bibliography

[1] John D Joannopoulos. *Photonic crystals: molding the flow of light*. Princeton University Press, Princeton, 2nd ed. edition, 2008. ISBN 978-0-691-12456-8. doi: 978-0-691-12456-8.

[2] Eli Yablonovitch and Eli Yablonovitch. Inhibited spontaneous emission in solid-state physics and electronics. *Physical Review Letters*, vol. 58(issue 20): 841–844, 1987. doi: 10.1007/978-1-4615-1963-8_41. Available from: http://link.aps.org/doi/10.1103/PhysRevLett.58.2059.

[3] Sajeev John. Strong localization of photons in certain disordered dielectric superlattices. *Physical Review Letters*, vol. 58(issue 23):2486–2489, 1987. ISSN 0031-9007. doi: 10.1103/PhysRevLett.58.2486. Available from: http://link.aps.org/doi/10.1103/PhysRevLett.58.2486.

[4] Thomas F. Krauss, Richard M. De La Rue, and Stuart Brand. Two-dimensional photonic-bandgap structures operating at near-infrared wavelengths. *Nature*, vol. 383(issue 6602):699–702, 1996-10-24. ISSN 0028-0836. doi: 10.1038/383699a0. Available from: http://www.nature.com/doifinder/10.1038/383699a0.

[5] Roman Antos, Vojtech Vozda, and Martin Veis. Plane wave expansion method used to engineer photonic crystal sensors with high efficiency. *Optics Express*, vol. 22(issue 3), 2014. doi: 10.1364/oe.22.002562. Available from: http://www.opticsinfobase.org/oe/abstract.cfm?uri=oe-22-3-2562.

[6] W. Axmann, P. Kuchment, and L. Kunyansky. Asymptotic methods for thin high-contrast two-dimensional pbg materials. *Journal of Lightwave Technology*, vol. 17(issue 11):1996–2007, 1999. doi: 10.1109/50.802986.

[7] Florin Abelés. La théorie générale des couches minces. pages 307–309. Available from: https://hal.archives-ouvertes.fr/jpa-00234261/document.

[8] D.H. Beckett, S.J. Cox, M. Molinari, J.M. Generowicz, B.P. Hiett, and K.S. Thomas. Application of finite element methods to photonic crystal modelling. *IEE Proceedings - Science, Measurement and Technology*, vol. 149(issue 5):293–296, 2002-09-01. ISSN 1350-2344. doi: 10.1049/ip-smt:20020642. Available from: http://digital-library.theiet.org/content/journals/10.1049/ip-smt_20020642.

[9] Kane Yee. Numerical solution of initial boundary value problems involving maxwell's equations in isotropic media. *IEEE Transactions on Antennas and Propagation*, vol. 14(issue 3):302–307, 1966. ISSN 0018-926x. doi: 10.1109/TAP.1966.1138693. Available from: http://ieeexplore.ieee.org/lpdocs/epic03/wrapper.htm?arnumber=1138693.

[10] S. T. Chu and S. K. Chaudhuri. Finite-difference time-domain method for optical waveguide analysis. *Prog. Electromagn. Res.*, vol. 11:255–300, 1995. Available from: http://www.jpier.org/PIER/pier.php?volume=11.

[11] Petr Malý. *Optika*. Karolinum, Praha, vyd. 1. edition, 2008. ISBN 978-80-246-1342-0.

[12] John B. Schneider. *Understanding the Finite-Difference Time-Domain Method*. 2012. Available from: http://www.eecs.wsu.edu/~schneidj/ufdtd/index.php.

[13] Atef Z Elsherbeni and Veysel Demir. *The finite-difference time-domain method for electromagnetics with MATLAB simulations*. SciTech Pub., Raleigh, NC, c2009. ISBN 04-712-1374-8.

[14] Allen Taflove and Susan C Hagness. *Computational electrodynamics*. Artech House, Boston, 3rd ed. / edition, c2005.

[15] Dennis M Sullivan and Susan C Hagness. *Electromagnetic simulation using the FDTD method*. Institute of Electrical and Electronics Engineers, New York: Institute of Electrical and Electronics Engineers, 3rd ed. / edition, c2000. ISBN 07-803-4747-1. Available from: http://www.dii.unipd.it/~alotto/download/file2.pdf.

[16] Ardavan F. Oskooi, David Roundy, Mihai Ibanescu, Peter Bermel, J.D. Joannopoulos, and Steven G. Johnson. Meep: A flexible free-software package for electromagnetic simulations by the fdtd method. *Computer Physics Communications*, vol. 181(issue 3):687–702, 2010. ISSN 00104655. doi: 10.1016/j.cpc.2009.11.008. Available from: http://math.mit.edu/~stevenj/papers/OskooiRo10.pdf.

[17] CALVIN D. SALZBERG and JOHN J. VILLA. Infrared refractive indexes of silicon germanium and modified selenium glass. *Journal of the Optical Society of America*, vol. 47(issue 3), 1957. doi: 10.1364/josa.47.000244.

[18] Jean-Pierre Berenger. A perfectly matched layer for the absorption of electromagnetic waves. *Journal of Computational Physics*, vol. 114(issue 2): 185–200, 1994. doi: 10.1006/jcph.1994.1159.

[19] K.S. Yee, Jei Shuan Chen, and A.H. Chang. Conformal finite-different time-domain (fdtd) with overlapping grids. *IEEE Transactions on Antennas and Propagation*, vol. 40(issue 9):1068–1075. ISSN 0018926x. doi: 10.1109/8.166532. Available from: http://ieeexplore.ieee.org/lpdocs/epic03/wrapper.htm?arnumber=166532.

[20] Richard Holland. Finite-difference solution of maxwell's equations in generalized nonorthogonal coordinates. *IEEE Transactions on Nuclear Science*, vol. 30(issue 6):4589–4591, 1983. ISSN 0018-9499. doi: 10.1109/tns.1983.4333176. Available from: http://ieeexplore.ieee.org/lpdocs/epic03/wrapper.htm?arnumber=4333176.

[21] Jinjie Liu, Moysey Brio, and Jerome V. Moloney. Overlapping yee fdtd method on nonorthogonal grids. *Journal of Scientific Computing*, vol. 39 (issue 1):129–143, 2009. ISSN 0885-7474. doi: 10.1007/s10915-008-9253-1. Available from: http://link.springer.com/10.1007/s10915-008-9253-1.

[22] R. Schuhmann and T. Weiland. Fdtd on nonorthogonal grids with triangular fillings. *IEEE Transactions on Magnetics*, vol. 35(issue 3):1470–1473. ISSN 00189464. doi: 10.1109/20.767244. Available from: http://ieeexplore.ieee.org/lpdocs/epic03/wrapper.htm?arnumber=767244.

[23] R. Nilavalan, I.J. Craddock, and C.J. Railton. Quantifying numerical dispersion in non-orthogonal fdtd meshes. *IEE Proceedings - Microwaves, Antennas and Propagation*, vol. 149(issue 1):23–27, 2002. doi: 10.1049/ip-map: 20020144.

[24] A Levi and Stephan Haas. *Optimal device design*. Cambridge University Press, New York, 2010. ISBN 05-211-1660-0.

[25] Wilhelm Magnus and Stanley Winkler. Hill's equation. doi: 0-486-49565-5.

[26] Francisco Guller, Marina E. Inchaussandague, and Ricardo A. Depine. Dispersion relation and band gaps of 3d photonic crystals made of spheres. *Progress In Electromagnetics Research M*, vol. 19:1–12, 2011. doi: 10.2528/pierm11051405.

[27] Keely J. Willis, John B. Schneider, and Susan C. Hagness. Amplified total internal reflection: theory, analysis, and demonstration of existence via fdtd. *Optics Express*, vol. 16(issue 3), 2008. doi: 10.1364/oe.16.001903.

[28] Orazio Svelto and D Hanna. *Principles of lasers*. Springer, New York, 5th ed. edition, 2009. ISBN 978-144-1913-012.

[29] Christopher Palmer and Erwin Loewen. *Diffraction grating handbook*. 705 St. Paul Street, Rochester, New York 14605 USA, 2005. Available from: http://optics.sgu.ru/~ulianov/Students/Books/Applied_Optics/E.%20Loewen%20Diffraction%20Grating%20Handbook%20(2005).pdf.

[30] Bahaa E. A.Malvin Carl Teich Bahaa E. A. Saleh. *Fundamentals of Photonics (Second Edition)*. Wiley-Interscience, New York, 1st ed. edition, 1991. ISBN 04-712-1374-8.

[31] Štefan Višňovský. Integrovaná a vlánová optika. 2015.

[32] Jigyasa Sharma and Asok De. Full-wave analysis of dielectric rectangular waveguides. *Progress In Electromagnetics Research M*, vol. 13:121–131, 2010. ISSN 1937-8726. doi: 10.2528/PIERM10051802. Available from: http://www.jpier.org/PIERM/pier.php?paper=10051802.

[33] E. A. J. Marcatili. Dielectric rectangular waveguide and directional coupler for integrated optics. *Bell System Technical Journal*, vol. 48(issue 7):2071–2102, 1969. doi: 10.1002/j.1538-7305.1969.tb01166.x.

[34] Max Born and Emil Wolf. *Principles of Optics*. Pergamon press, Headington Hill Hall, Oxford, fourth edition edition, 1970.

[35] Nina Skivesen, Amélie Têtu, Martin Kristensen, Jørgen Kjems, Lars H. Frandsen, and Peter I. Borel. Photonic-crystal waveguide biosensor. *Optics*

Express, vol. 15(issue 6):3169–, 2007. ISSN 1094-4087. doi: 10.1364/OE. 15.003169. Available from: http://www.opticsinfobase.org/abstract. cfm?URI=oe-15-6-3169.

[36] H. Kurt, D. Yilmaz, A. E. Akosman, and E. Ozbay. Asymmetric light propagation in chirped photonic crystal waveguides. *Optics Express*, vol. 20(issue 18):20635–, 2012. ISSN 1094-4087. doi: 10.1364/OE.20.020635. Available from: http://www.opticsinfobase.org/abstract.cfm?URI=oe-20-18-20635.

[37] Shanhui Fan, J. D. Joannopoulos, Joshua N. Winn, Adrian Devenyi, J. C. Chen, and Robert D. Meade. Guided and defect modes in periodic dielectric waveguides. *Journal of the Optical Society of America B*, vol. 12(issue 7): 1267–995, 1995. doi: 10.1364/josab.12.001267.

[38] G. W. Burr, S. Diziain, and M.-P. Bernal. The impact of finite-depth cylindrical and conical holes in lithium niobate photonic crystals. *Optics Express*, vol. 16(issue 9), 2008. doi: 10.1364/oe.16.006302.

List of Abbreviations

ABC   Absorbing Boundary Conditions
ADE   Auxiliary Differential Equation
CFL   Courant-Friedrichs-Lewy condition
CPML   Convolutional PML
DFT   Discrete Fourier transform
EM   Electromagnetism
FD   Fresnel Diffraction
FDTD   Finite Difference Time Domain
FWHM Full Width At Half Maximum.
NTFF   Near-To-Far-Field transformation
PhC   Photonic Crystal
PML   Perfectly Matched Layer
PWE   Plane Wave Expansion
RI   Refractive Index
RIU   Refractive Index Unit
QM   Quantum Mechanics
SPR   Surface Plasmon Resonance
TFSF   Total-Field/Scattered-Field
TMM   Transfer Matrix Method

Appendix: Bare-bone FDTD code

Here is the matlab code of bare-bone FDTD simulation. Gaussian pulse is excited at node 30 of total 100 and the update equations are integrated over 500 time-steps afterwards.

```matlab
1  % Bare-bone FDTD simulation
2  clear all; clc; close all;      % clear workspace
3
4  eps0 = 8.854187817e-12;         % permittivity of free space
5  mu0  = 4*pi*1e-7;               % permeability of free space
6  c    = 1/sqrt(mu0*eps0);        % speed of light
7
8  dx = 10e-9;                 % 10 nanometers between each two nodes
9  dt = dx/c;                  % Courant-Friedrichs-Lewy condition
10
11 sizeX = 100;               % number of nodes, real size is sizeX*dx
12 Ez = zeros(sizeX,1);       % allocate empty array for electric field
13 Hy = zeros(sizeX-1,1);     % allocate empty array for magnetic field
14
15 width = 10;                % temporal width of Gaussian pulse
16 delay = 5*width;           % temporal delay of Gaussian pulse
17
18 animFig = figure;          % open figure for animated output
19
20 maxTime = 500;             % number of time-steps
21 for time = 1 : maxTime     % time marching loop
22
23     % update magnetic field using update equation
24     for i = 1 : sizeX-1
25         Hy(i) = Hy(i)+(2*dt/dx)/(2*mu0)*(Ez(i+1)-Ez(i));
26     end
27
28     % update electric field using update equation
29     for i = 2 : sizeX-1
30         Ez(i) = Ez(i)+(2*dt/dx)/(2*eps0)*(Hy(i)-Hy(i-1));
31     end
32
33     % excite Gaussian pulse into the Yee grid at node 30
34     arg = (time-delay)/width;
35     Ez(30) = exp(-arg*arg);
36
37     % plot animation
38     figure(animFig);                  % activate animation figure
39     plot(Ez);                         % plot electric field
40     axis([1 sizeX -2 2]);             % set limits
41     pause(0.01);                      % slow down the animation
42
43 end
```

The printed version of this work is accompanied by a CD, where full FDTD code is recorded.